



## Dual optimization approach to Mo single atom dispersed g-C<sub>3</sub>N<sub>4</sub> photocatalyst: Morphology and defect evolution

Chen Zhang<sup>a,b,\*</sup>, Deyu Qin<sup>a,b</sup>, Yin Zhou<sup>a,b</sup>, Fanzhi Qin<sup>a,b</sup>, Hou Wang<sup>a,b</sup>, Wenjun Wang<sup>a,b</sup>, Yang Yang<sup>a,b</sup>, Guangming Zeng<sup>a,b,\*</sup>

<sup>a</sup> College of Environmental Science and Engineering, Hunan University, Changsha 410082, PR China

<sup>b</sup> Key Laboratory of Environmental Biology and Pollution Control, Hunan University, Ministry of Education, Changsha 410082, PR China

### ARTICLE INFO

#### Keywords:

Tubular g-C<sub>3</sub>N<sub>4</sub>  
N vacancy  
Mo single atom photocatalysts  
DFT calculations  
Tetracycline degradation

### ABSTRACT

Reasonable regulation of the interaction between metal center and the ligand to achieve a high-density atomic loading without agglomeration has been the formidable challenge to the development of single-atom catalysts (SACs). Herein, an advanced photocatalyst based on N-vacancy (Nv) tubular porous g-C<sub>3</sub>N<sub>4</sub> (TCN) decorated with atomically dispersed Mo (Mo/Nv-TCN) is synthesized. The large specific surface area of the tubular morphology contributes to suppress the agglomeration of Mo atoms, while the N defect induces the formation of specific stable Mo-2 C/2 N configuration between the light absorbers and the Mo sites. As the active center of the photocatalytic reaction, single Mo atom causes the directional transfer of local charges on the surface of the support, while the Mo-2 C/2 N bond acts as a bridge for photoexcited charge transfer. As a result, the precisely designed Mo SACs system shows remarkable photoelectric properties and renders excellent photocatalytic performance for tetracycline (TC) degradation under visible light irradiation.

### 1. Introduction

Tetracycline (TC), as a common human and animal antibiotic, has been widely used in the medical and feed industries for many years [1, 2]. In general, tetracycline is difficult to be completely metabolized in organisms, leading to its frequent detection in the environment, which inevitably causes environmental pollution [3,4]. In addition, TC can induce the production of many antibiotic resistance genes and resistant bacteria in the process of clinical application, so it has a great ecological risk [5–7]. Therefore, it is necessary to seek advanced and eco-friendly TC degradation technology. In recent years, as a promising advanced oxidation process, photocatalysis has received extensive attention in the field of degradation of antibiotics [8–10]. The application of a variety of different photocatalysts (such as CdS, TiO<sub>2</sub>, ZnO, and Fe<sub>2</sub>O<sub>3</sub>, etc.) has received a lot of research and exploration [11–15]. Since Wang et al. used graphitic carbon nitrides (g-C<sub>3</sub>N<sub>4</sub>) for photocatalytic hydrogen evolution in 2009 [16], series of excellent properties of g-C<sub>3</sub>N<sub>4</sub> have been well applied in the field of photocatalysis, such as high stability, easy preparation, low toxicity, suitable band structure and so on [17–19]. Nevertheless, the application of g-C<sub>3</sub>N<sub>4</sub> has been restricted by its shortcomings such as poor visible light absorption, easy

recombination of photogenerated charge carriers, and limited active sites [20].

Recently, the design concept of single atom catalysts (SACs) has gradually become a research frontier in the field of catalytic materials. Unlike traditional nanoclusters, the metals in SACs are supported on the surface of the material in the form of atomic dispersion, and there is no mutual contact between adjacent atoms in theory [21]. The specific coordination relationship is formed between the single metal atom and the carrier, which exhibits a unique electronic structure. In addition, SACs can provide as many active sites as possible by maximizing exposure of low-coordination metal atoms [22]. In short, SACs is an economical and efficient catalyst design concept. As an excellent photocatalyst, g-C<sub>3</sub>N<sub>4</sub> (CN) is a suitable carrier for SACs. The collision of g-C<sub>3</sub>N<sub>4</sub> and single atoms can produce dazzling sparks in the field of photocatalysis. For instance, Li et al. used H<sub>2</sub>PtCl<sub>6</sub> as the Pt source, and successfully loaded Pt single atoms on the surface of g-C<sub>3</sub>N<sub>4</sub> through liquid phase reaction and low-temperature annealing [23]. The stable coordination structure was formed by Pt-C/N bond, which had high photocatalytic H<sub>2</sub> evolution efficiency. Besides, Yang and co-workers anchored single-atom Co on g-C<sub>3</sub>N<sub>4</sub> by means of Co-O and Co-N bonds, which effectively improve the photoelectric properties of the

\* Corresponding authors at: College of Environmental Science and Engineering, Hunan University, Changsha 410082, PR China.

E-mail addresses: [zhangchen@hnu.edu.cn](mailto:zhangchen@hnu.edu.cn) (C. Zhang), [zgming@hnu.edu.cn](mailto:zgming@hnu.edu.cn) (G. Zeng).

<https://doi.org/10.1016/j.apcatb.2021.120904>

Received 12 September 2021; Received in revised form 18 October 2021; Accepted 3 November 2021

Available online 7 November 2021

0926-3373/© 2021 Elsevier B.V. All rights reserved.

material [24]. Similarly, Sharma found that the Ru-N/C bond between single-atom Ru and modified g-C<sub>3</sub>N<sub>4</sub> can accelerate charge transfer and prolong the lifetime of carriers, thereby enhancing the ability of photocatalytic reduction of CO<sub>2</sub> [25]. Currently, the single atom metals that have received widespread attention mainly include Pt, Co, Pd, Au, Cu, and so on [26–30]. Molybdenum (Mo), as a common transition metal element, has a series of advantages such as easy preparation, low price, stable properties, and low toxicity. Mo-based materials have been widely studied in the fields of electrode and catalysis due to their chemical inertness and excellent electrochemical performance [31–33]. Related studies have proved that the non-noble metal Mo element has a good effect in the direction of SACs, such as application in electrocatalysis and electrode materials, and its application in the field of photocatalysis has gradually been discovered [34–36]. At present, a small amount of research has proved that single-atom Mo can form Mo-C/N or double-N (Mo-N<sub>2</sub>) coordination structure with g-C<sub>3</sub>N<sub>4</sub> [37, 38].

To ensure the high dispersion and stable loading of single atom Mo, new simple synthesis methods and a series of modification measures are worthy of further exploration. For SACs, metal agglomeration and low dense atom dispersion have always been the major problem restricting its development, but in general, these problems can be effectively alleviated through the modification of the support. For example, Cheng et al. prepared porous graphene oxide rich in surface defects by microwave exfoliation [39]. The defects at the pore edges provided abundant anchoring sites for single atom Ni, and the loading of Ni atoms was as high as 6.9 wt%. When g-C<sub>3</sub>N<sub>4</sub> is used as a support, reasonable modification of g-C<sub>3</sub>N<sub>4</sub> is also an effective means to improve the association between ligand and atomic catalytic sites. Firstly, by rationally designing the morphology of the support, it will have a larger specific surface area [40], so as to provide more loading sites for the dispersed atoms. Through proper control of the synthesis process of g-C<sub>3</sub>N<sub>4</sub>, some special morphologies can be cleverly constructed, such as nanosheet [41], nanorod [42], nanotube [43], microsphere [44], and flower-like [45], etc. Secondly, the electronic structure and physicochemical properties of the supports surface can be changed by defect engineering. By constructing defect sites on the surface of the support, a specific coordination structure can be generated between the single atom and the support, thereby promoting the stability and dispersibility of the anchoring of the single atom. Regarding g-C<sub>3</sub>N<sub>4</sub>, the C/N vacancy can be

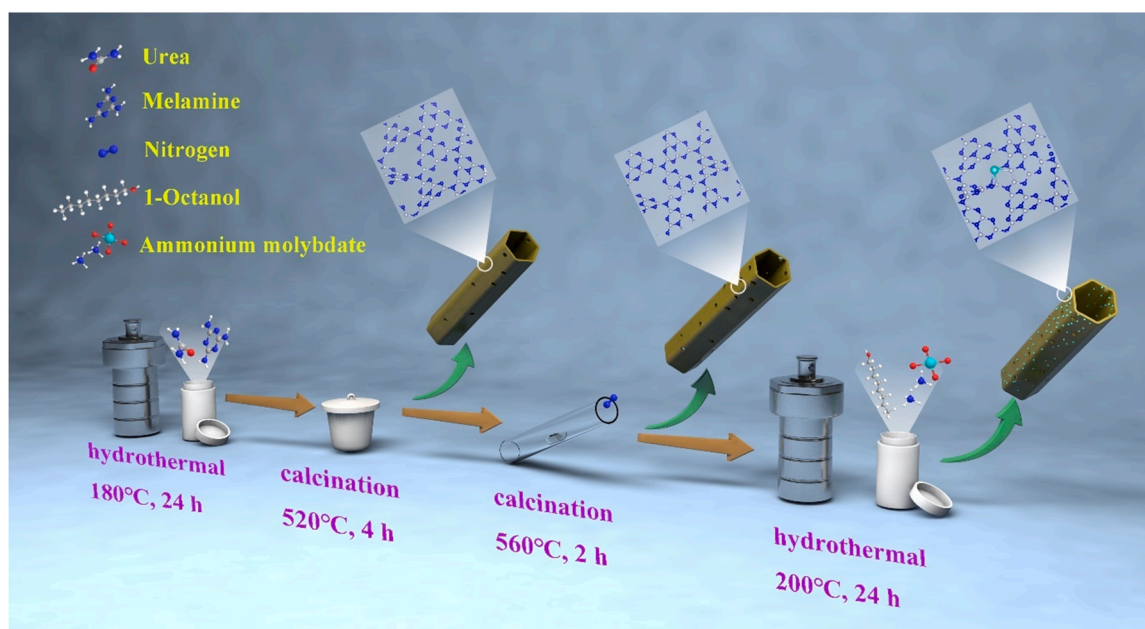
generated through the adjustment of the traditional synthesis method or the reprocessing of the sample, and then some unusual coordination between the g-C<sub>3</sub>N<sub>4</sub> and the single atom can be formed to produce a better photoelectric effect [46,47].

Herein, g-C<sub>3</sub>N<sub>4</sub> is selected to be a support material for SACs due to its easy modification and favorable photocatalytic performance. We optimize the structure and properties of the pristine g-C<sub>3</sub>N<sub>4</sub> through morphology and defect engineering, and prepare tubular porous g-C<sub>3</sub>N<sub>4</sub> (TCN) with N vacancies (Nv-TCN). The larger specific surface area of the tubular morphology provides more sites for the loading of atoms, and the introduction of N defects enables the formation of a special stable structure between the ligand and the single atom. In this work, with Nv-TCN as the carrier, single atom Mo is anchored on its surface through a facile solvothermal synthesis strategy (Scheme 1). Atomic characterization and density functional theory (DFT) calculations proves that single-atom Mo and Nv-TCN are connected by Mo-C and Mo-N bonds to form a stable Mo-2 C/2 N coordination structure. The anchoring of atomic Mo can enhance the visible light absorption capacity of g-C<sub>3</sub>N<sub>4</sub>, accelerate the separation and transfer of photogenerated charge carriers, and increase the charge density. The incorporation of atomic Mo leads to a directional transfer of local charges on the surface of Nv-TCN, and the Mo-2 C/2 N bond acts as a bridge for charge transfer. The Mo atom becomes the active center of the photocatalytic reaction. Thanks to the above positive effects, the photodegradation activity of the sample to TC can be greatly improved under visible light conditions.

## 2. Experimental section

### 2.1. Reagents

In this experiment, all reagents involved in this experiment were of unpurified analytical grade. TC, urea (CO(NH<sub>2</sub>)<sub>2</sub>), melamine (C<sub>3</sub>N<sub>3</sub>(NH<sub>2</sub>)<sub>3</sub>), ammonium molybdate ((NH<sub>4</sub>)<sub>6</sub>Mo<sub>7</sub>O<sub>24</sub>·4 H<sub>2</sub>O), 1-octyl alcohol (C<sub>8</sub>H<sub>18</sub>O), 4-hydroxy-2,2,6,6-tetramethylpiperidinyloxy (TEM-POL), disodium oxalate (Na<sub>2</sub>C<sub>2</sub>O<sub>4</sub>), L-tryptophan (C<sub>11</sub>H<sub>12</sub>N<sub>2</sub>O<sub>2</sub>), and isopropanol (IPA, C<sub>3</sub>H<sub>8</sub>O) were supplied from Sinopharm Corporation Ltd. (Shanghai, China).



**Scheme 1.** Schematic illustration for the preparation of Mo/Nv-TCN.

## 2.2. Synthesis of photocatalysts

Synthesis of bulk CN: In a covered crucible, melamine was heated to 550 °C at a rate of 2.3 °C/min and kept calcined for 4 h. Then, the sample was cooled to room temperature naturally.

Synthesis of TCN: The synthesis of TCN was based on the preparation method published by our group [48]. First, 8 g of urea, 6 g of melamine and 70 mL of deionized water were placed in a 100 mL Teflon-lined stainless-steel autoclave and stirred for about 15 min. Then the mixed solution was hydrothermally heated at 180 °C for 24 h, and the prepared precursor was washed several times and dried. Finally, the dried white sample was heated to 550 °C at a rate of 2.3 °C/min and calcined for 2 h. After cooling, the yellow TCN powder can be obtained.

Synthesis of Nv-TCN: 1 g of TCN was reheated to 560 °C for 2 h at a rate of 2 °C/min in N<sub>2</sub> atmosphere [49]. After the sample was cooled naturally, the yellow powder was collected to obtain TCN with N vacancies, noted as Nv-TCN.

Synthesis of Mo/Nv-TCN: 0.3 g of Nv-TCN and a certain amount of ammonium molybdate (1, 5, 10, 15 and 20 mg) were added to 30 mL of 1-octyl alcohol and stirred for 15 min. In a Teflon-lined stainless-steel autoclave, the mixture undergoes solvothermal reaction for 24 h at 200 °C. Then, the cooled mixture was washed several times. Finally, the single atom Mo loaded Nv-TCN was obtained by drying the products at 60 °C for 12 h. The samples were denoted as 1-Mo/Nv-TCN, 5-Mo/Nv-TCN, 10-Mo/Nv-TCN, 15-Mo/Nv-TCN, and 20-Mo/Nv-TCN, respectively. Through inductively coupled plasma mass spectrometry (ICP-MS, Agilent 7700), the Mo content in Nv-TCN was measured to be 0.11, 0.48, 1.21, 2.01, and 2.92 wt%, respectively.

## 2.3. Characterization

The morphologies of the samples were acquired on Zeiss Sigma 300 Scanning electron microscopy (SEM). Transmission electron microscopy (TEM) and energy disperse X-ray spectroscopy (EDS) mapping profiles were obtained on FEI Tecnai F20 to characterize the microstructure and elemental distribution of the samples. Aberration-corrected high-angle-annular-dark-field scanning transmission electron microscopy (HAADF-STEM, EI Themis Z) was used to verify the dispersion of single atom. Brunauer-Emmett-Teller (BET) and Barrett-Joyner-Halenda (BJH) method were measured by a Micromeritics ASAP 2020 HD88 instrument. The X-ray diffraction (XRD) was characterized by Panalytical Empyrean powder diffractometer with Cu K $\alpha$  radiation (The scanning range is from 10° to 80°). The Fourier transform infrared (FT-IR) spectra was obtained by the Thermo Scientific Nicolet iS5 spectrophotometer with KBr pellet method. Electron paramagnetic resonance (EPR) was acquired by the EPR spectrometer (JEOL JES-FA200). The contents of C and N elements were obtained by elemental analysis (EA, Vario MACRO cube analyzer). X-ray photoelectron spectroscopy (XPS) was measured using the Thermo Scientific K-Alpha spectrometer with Al K $\alpha$  line source. The X-ray absorption near-edge structure (XANES) and extended X-ray absorption fine structure (EXAFS) of the sample at Mo K-edge was performed on the Beamline of TLS07A1 (National Synchrotron Radiation Research Center, Taiwan). Furthermore, the data of XANES and EXAFS were analyzed by Athena and Artemis software packages. UV-visible diffused reflectance spectra (UV-vis DRS) were determined by a Varian Cary 300 instrument. Photoluminescence (PL) emission spectra and time-resolved photoluminescence (TRPL) decay spectra were monitored by the Fluoromax-4 spectrophotometer and FLS1000 fluorescence lifetime spectrophotometer, respectively. Electron spin response (ESR) of reactive species were measured on a Bruker A300 spectrometer. The content of Mo in the samples was performed by the ICP-MS on Agilent 7700.

## 2.4. Photoelectrochemical test

Electrochemical impedance spectroscopy (EIS), Mott-Schottky plots,

and photocurrent density of the materials were measured by electrochemical workstation with a three-compartment electrochemical cell (Chenhua CHI 760E). The Pt wire and Ag/AgCl electrode were used as counter electrode and reference electrode, respectively. The electrolyte was 0.2 M Na<sub>2</sub>SO<sub>4</sub> solution. Fluorine-doped tin oxide (FTO) glass plates (1 cm × 2 cm) were used to attach the samples as working electrode, and the specific preparation method was as follows: Firstly, the glass plates were ultrasonically cleaned sequentially with acetone, ethanol, and deionized water. Then, 5 mg of sample powder and 1 mL of 20% nafion solution were mixed by ultrasonic dispersion. Next, the mixture was dropped into a 1 cm<sup>2</sup> effective working area of the glass plates, and the samples was heated at 120 °C for 2 h. A 300 W xenon lamp (PLS-SXE300/300 UV) with a 420 nm cutoff filter was used to simulate visible light.

## 2.5. Photocatalytic performance evaluation

The degradation efficiency of TC was used as the index to measure the photocatalytic performance of samples. The visible light was simulated by a 300 W xenon lamp (PLS-SXE300/300 UV), which used a glass filter to remove the ultraviolet light with a wavelength below 420 nm. Typically, 50 mg photocatalyst was added to 50 mL TC solution and stirred for 60 min under dark conditions to achieve an adsorption-desorption equilibrium. Under simulated visible light irradiation, 2 mL of the mixture was sampled at intervals of 15 min. The TC solution and the photocatalyst were separated by a 0.22  $\mu$ m filter membrane. The concentration of the TC aqueous solution was measured by high performance liquid chromatography (HPLC, Agilent 1260 Infinity II, USA) with an EC-C18 column (4.6 × 150 mm). The column temperature was 25 °C and the detection wavelength was 280 nm. The volume ratio of 0.01 M oxalic acid aqueous solution to acetonitrile in the mobile phase was 4:1, and the flow rate was 1 mL min<sup>-1</sup>. The sample volume was 20  $\mu$ L for each injection. The formula for calculating the photocatalytic degradation efficiency ( $\eta$ , %) of TC is as follows:

$$\eta = \frac{C_0 - C_t}{C_0} \times 100\% \quad (1)$$

Where C<sub>0</sub> represents the initial TC concentration, while C<sub>t</sub> represents the TC concentration after t min degradation. The intermediate products were analyzed via the liquid chromatography coupled with tandem mass spectrometry (LC-MS/MS) technology (The specific experimental details can be found in the Text S1). In order to measure the stability of the photocatalyst, the used sample was washed with ethanol and ultrapure water, and then filtered and dried. The collected dry samples were cyclically tested in accordance with the above-mentioned method. The total organic carbon (TOC) content was detected by Shimadzu TOC-L analyzer.

Moreover, to explore the mechanism of photocatalytic degradation, the contribution of reactive species was identified by trapping experiment. In this experiment, IPA (10 mM), Na<sub>2</sub>C<sub>2</sub>O<sub>4</sub> (10 mM), TEMPOL (10 mM), and L-tryptophan (10 mM) acted as the quenching agents of •OH, h<sup>+</sup>, •O<sub>2</sub><sup>-</sup>, and <sup>1</sup>O<sub>2</sub>, respectively.

## 2.6. Theoretical computation

The coordination structure of the materials were optimized using the Vienna Ab-initio Simulation Package (VASP) [50,51] with the frozen-core all-electron projector-augment-wave (PAW) [52,53] method. The exchange and correlation potential were evaluated by the Perdew-Burke-Ernzerhof (PBE) [54] of generalized gradient approximation (GGA). The cutoff energy for the plane-wave basis set was 450 eV. The Monkhorst-Pack k-point [55] sampling was set to 3 × 1 × 1 for monolayer g-C<sub>3</sub>N<sub>4</sub>. A vacuum region of 20 Å was added above monolayer g-C<sub>3</sub>N<sub>4</sub> to minimize the interactions between neighboring systems. The coordination structure optimizations were carried out until

the forces on each ion was reduced below 0.01 eV/Å.

The formation energies ( $E_{\text{form}}$ ) of N-vacancy were calculated by the Eq. (2):

$$E_{\text{form}} = E(\text{vacancy}) - E(\text{pure}) + \mu(\text{N}) \quad (2)$$

where  $E(\text{vacancy})$  and  $E(\text{pure})$  represent the total energies of N-vacancy and pristine  $\text{C}_3\text{N}_4$ , respectively.  $\mu(\text{N})$  represents the chemical potentials of N atom.

The adsorption energy ( $E_{\text{ads}}$ ) was calculated by the Eq. (3):

$$E_{\text{ads}} = E_{\text{Mo+surface}} - E_{\text{surface}} - E_{\text{Mo}} \quad (3)$$

where  $E_{\text{surface}}$  is the energy of  $\text{C}_3\text{N}_4$ ,  $E_{\text{Mo}}$  is the energy of the Mo atom, and  $E_{\text{Mo+surface}}$  is the total energy of the Mo/CN compound.

In addition, the Fukui function based on Gaussian 16 [56], Revision A.03 and Multiwfn 3.7 [57] was used to analyze the active sites of materials and the tendency of internal electron transfer. On the other hand, it was also used to analyze the sites where TC molecules are vulnerable to attack by active species, thus supporting the degradation pathway of TC. The geometry optimizations are conducted using the B3LYP functional [58,59], with LanL2DZ pseudopotential basis set [60,61] for Mo atom and 6–31 G (d) basis set for the other atoms. Moreover, in order to better describe the weak interactions among molecules, DFT-D dispersion correction is added to the calculation. In TC calculation, the solvation effect is considered and PCM implicit solvation model was adopted. It should be noted that although the methods and basis sets selected in this study are of low accuracy, they are completely sufficient for the calculation of Fukui function for qualitative analysis and reactive site prediction. The specific calculation details can be found in the Text S2.

### 3. Results and discussion

#### 3.1. Physicochemical and electronic properties

The morphologies and structure of different materials were detected by SEM and TEM. From Fig. 1a and e, CN shows an irregular blocky structure. After the pretreatment of the precursor, the prepared TCN formed obvious tubular morphology (Fig. 1b). In addition, the different shadow distribution shown by TEM image in Fig. 1f confirms the hollow structure in the tube again. Similarly, Fig. 1c and g show the same hollow tubular structure as TCN, indicating that the introduction of N vacancy does not damage the morphology of the sample basically. In the process of single atom solvothermal loading, Mo atoms on the surface of Nv-TCN do not accumulate together, and regular tubular structures can still be observed by SEM (Fig. 1d) and TEM (Fig. 1h). EDS elemental mapping images (Fig. 1i) exhibits that Mo elements are as uniformly dispersed as C and N elements. In order to further confirm that Mo is anchored on the surface of Nv-TCN in the form of atomic dispersion, HAADF-STEM was used for the characterization of 10-Mo/Nv-TCN samples. As shown in Fig. 1j, the bright dots represent the atomic-sized Mo elements. These bright spots are distributed uniformly and isolated on the surface of the carrier, which proves the successful preparation of Mo single atoms. Considering that this study involved the optimization of morphology,  $\text{N}_2$  adsorption-desorption isotherms and BJH pore size distribution were used to reflect the influence of morphological changes. In Fig. 1k, type IV adsorption curves appear in all the different samples, indicating that the materials had mesoporous structure. The pore size of the pristine CN is extremely small due to its bulk structure, while the modified tubular  $\text{g-C}_3\text{N}_4$  generally has a larger

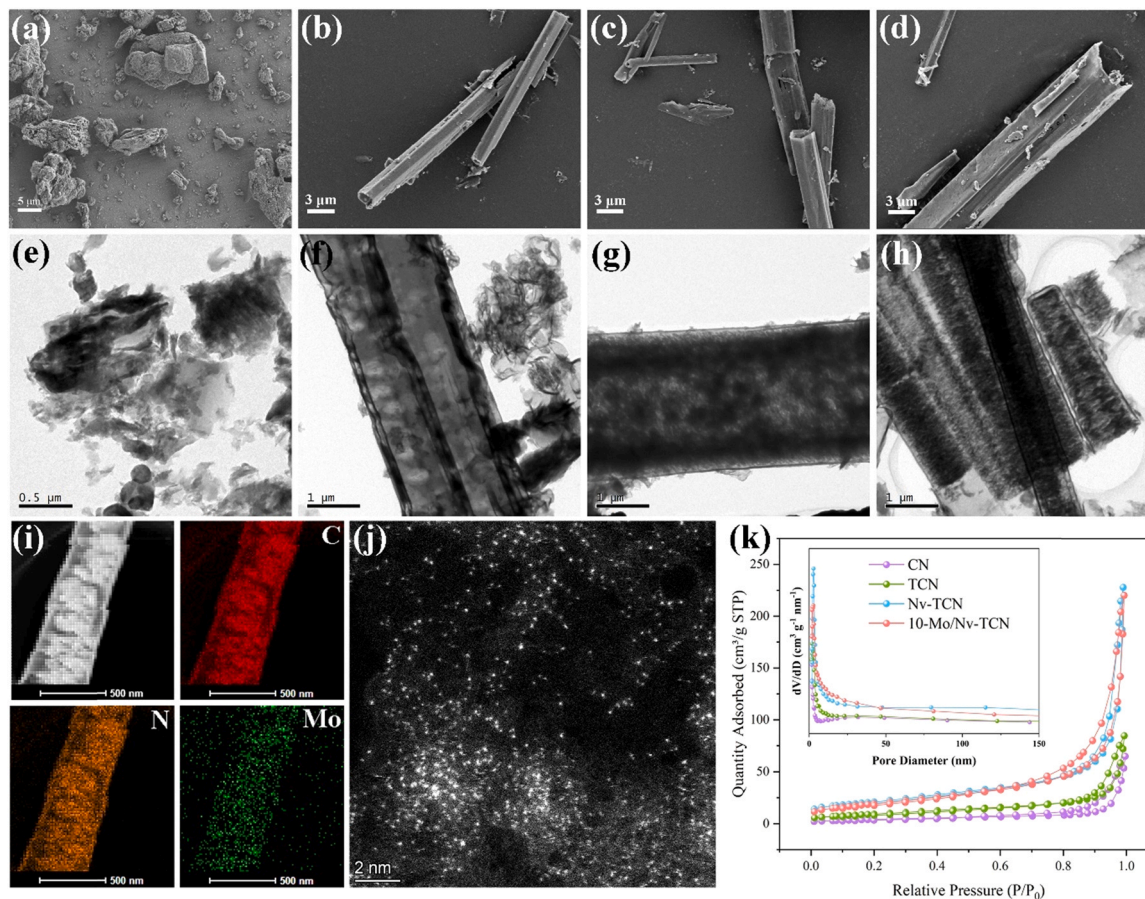


**Fig. 1.** SEM images of a) CN, b) TCN, c) Nv-TCN and d) 10-Mo/Nv-TCN. TEM images of e) CN, f) TCN, g) Nv-TCN, and h) 10-Mo/Nv-TCN. i) EDS elemental mapping images of 10-Mo/Nv-TCN. j) HAADF-STEM images of 10-Mo/Nv-TCN. k) Nitrogen adsorption-desorption isotherms and the pore size distribution curves (inset).

pore size. In addition, the BET specific surface areas of CN, TCN, Nv-TCN, and 10-Mo/ Nv-TCN are 16.20, 34.17, 74.22, and 73.53 m<sup>2</sup>/g, respectively. In conclusion, the directional design of g-C<sub>3</sub>N<sub>4</sub> morphology in this experiment significantly increases the specific surface area and optimizes the pore size distribution of the sample, thus providing more anchoring sites for single atoms. Besides, this feature also facilitates light absorption and mass transfer.

The crystal structures of different samples were reflected in Fig. 2a by XRD patterns. Typically, all the samples have characteristic peaks located at 13.0° and 27.5°, corresponding to the (100) and (002) crystal planes of g-C<sub>3</sub>N<sub>4</sub>, which can be attributed to the in-plane packed tri-s-triazine units and the graphene-like  $\pi$ - $\pi$  layer stacking, respectively [62]. After morphology modification and the introduction of defects, no new characteristic peaks are generated or missing in XRD patterns, which means that TCN and Nv-TCN still maintain the basic crystal structure of bulk CN. The intensity and position of characteristic peaks in the spectrum did not change before and after the loading of atom Mo, indicating the low loading of Mo, and no new compounds such as Mo<sub>2</sub>C were generated [63]. The peak density of CN at the position of 27.5° is obviously stronger than that of other samples, which is due to the size effect caused by the ultrathin tubular structure, which affects the stacking structure in the layer [64]. Fig. 2b lists the FT-IR spectra of each sample to further compare their chemical molecular structures. All samples have obvious peaks at approximately 810, 1200–1750, and 3000–3400 cm<sup>-1</sup>. Among them, the peak around 810 cm<sup>-1</sup> represents the out-of-plane bending mode of the triazine units. The absorption peak between 1200 and 1750 cm<sup>-1</sup> and 3000–3400 cm<sup>-1</sup> corresponds to the stretching vibrations mode of C-N heterocycles and N-H in bridged or terminal amine groups [65]. The characteristic peaks of different samples remain unchanged, which demonstrates that neither the tubular morphology nor the N vacancy will have a great influence on the microstructure of bulk CN, while Mo exists in the form of single atom and does not change the molecular structure of CN. These conclusions are consistent with the results of XRD patterns.

In this study, N vacancy was introduced by gas etching. Since the stability of different bonds in TCN molecules is different, calcination under N<sub>2</sub> conditions will lead to the cleavage of some specific bonds, resulting in the escape of N atoms from the lattice at specific positions and the formation of N vacancies. Some characterization was carried out to verify the successful introduction of N vacancies in the synthesis process. From the EPR spectrum shown in Fig. 3a, it can be seen that TCN and Nv-TCN all show single Lorentzian line at the g-value of 2.003. By comparison, it can be seen that Nv-TCN has a significantly stronger peak intensity than TCN, which is related to the unpaired electrons of the C atom in the  $\pi$ -conjugated aromatic rings [66]. This stronger peak

density can indicate that a certain amount of surface vacancies are formed on the surface of Nv-TCN, which increases the number of unpaired electrons [67]. In order to further determine the type of surface vacancy, EA analysis was performed to compare the atomic ratios of C and N in different samples (Fig. 3b). Through organic element analysis, C/N in CN, TCN and Nv-TCN are 0.566, 0.571 and 0.596, respectively. This indicates that the ratio of C/N in both CN and TCN samples is close to each other, while a certain proportion of N atoms is missing in Nv-TCN samples. Similar results were reflected in the XPS data, the XPS analysis shows that the C/N of the above three are 0.471, 0.482, and 0.571, respectively. Although XPS data is not very accurate, its trend is consistent with the results of EA, which can be used as a corroboration of EA data. The increase of the value of C/N indicates that the defects generated in Nv-TCN should belong to N vacancy. The data in Fig. 3c are derived from the N element high-resolution spectra in XPS analysis of Nv-TCN samples. The C=N-C peak areas of CN and TCN are 111438.3 eV and 101617.6 eV, respectively, which decrease to 68657.2 eV after the introduction of vacancy (Nv-TCN). As a semi-quantitative technique, the peak area data of XPS may not be particularly accurate, but this result can be used as a preliminary estimate of the N-vacancy generated at the N-2 C coordination position of g-C<sub>3</sub>N<sub>4</sub>. To obtain more accurate information of N vacancy, the total energy of Nv-TCN in defect state and the formation energy of Nv-2 C (Fig. 3d), Nv-3 C<sub>1</sub> (Fig. 3e) and Nv-3 C<sub>2</sub> (Fig. 3f) vacancy were calculated by DFT. The total energies of Nv-2 C-TCN, Nv-3 C<sub>1</sub>-TCN, and Nv-3 C<sub>2</sub>-TCN are -940.66, -938.58, and -939.91 eV, respectively. In general, the lower the energy of a substance, the more stable its structure. Therefore, the structure of Nv-2 C-TCN is more ideal than Nv-3 C<sub>1</sub>-TCN and Nv-3 C<sub>2</sub>-TCN. Based on the total energy of pure g-C<sub>3</sub>N<sub>4</sub> (-950.91 eV) and the chemical potential of N atom (-8.31 eV), the formation energies of Nv-2 C, Nv-3 C<sub>1</sub> and Nv-3 C<sub>2</sub> were calculated to be 1.94, 4.02, and 2.69 eV, respectively. The lowest formation energy means that Nv-2 C is most likely to be generated, which is consistent with the results of XPS, indicating that Nv-2 C type vacancies are mainly formed in Nv-TCN.

XPS analysis was used to characterize the influence of morphology control, vacancies, and single atom Mo on the chemical state and composition of g-C<sub>3</sub>N<sub>4</sub>. It can be seen from Fig. 4a and Fig. S1a that only C, N, and O are contained in the survey spectrum of TCN and Nv-TCN, which is consistent with bulk CN. However, the 10-Mo/Nv-TCN sample produces a significant new peak corresponding to Mo element, which means that the Mo atom is successfully anchored to the surface of Nv-TCN. The peaks of the C1s element high-resolution spectrum in CN (Fig. S1b) at 284.8, 285.7, and 287.9 eV correspond to adsorbed hydrocarbons, sp<sup>3</sup>-coordinated C, and sp<sup>2</sup> hybridized C from the N-C=N

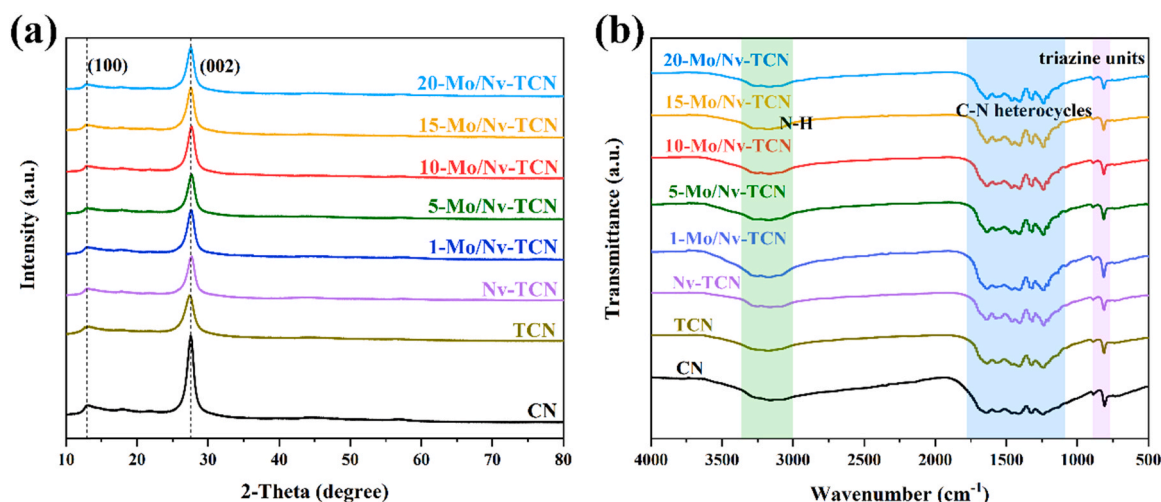


Fig. 2. a) XRD patterns and b) FT-IR spectra of the different samples.

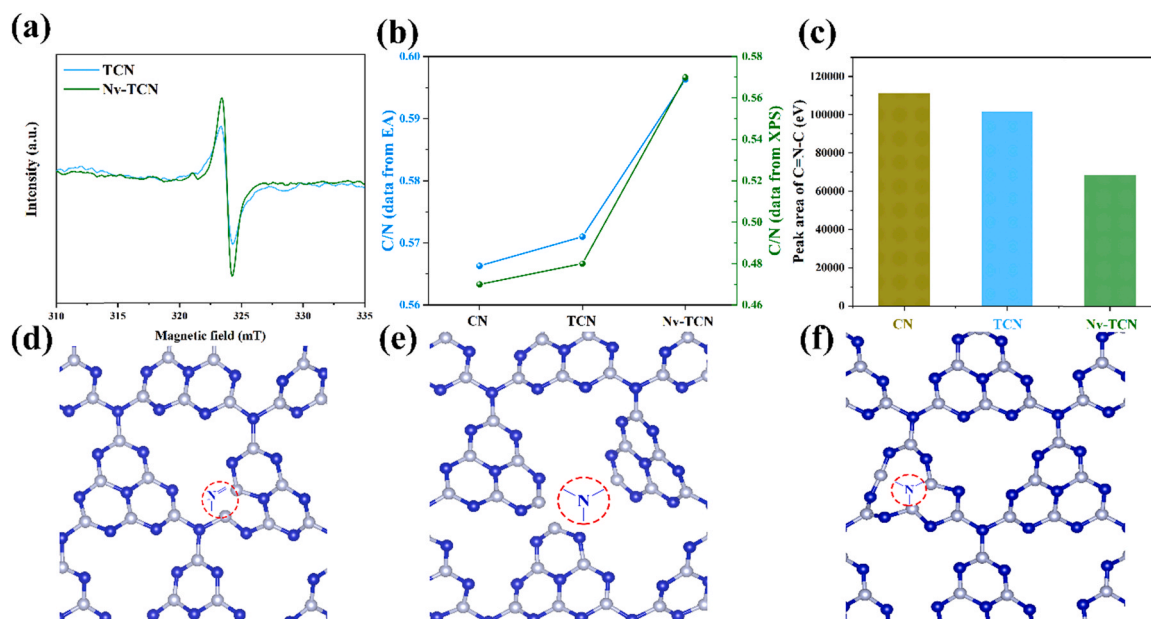


Fig. 3. a) EPR spectra of samples. b) C/N atomic ratio of samples from EA and XPS. c) The peak area of C=N-C from XPS. The schematic diagram of three different N vacancies in carbon nitride: d) Nv-2 C, e) Nv-3 C<sub>1</sub>, and f) Nv-3 C<sub>2</sub> (gray, carbon; blue, nitrogen).

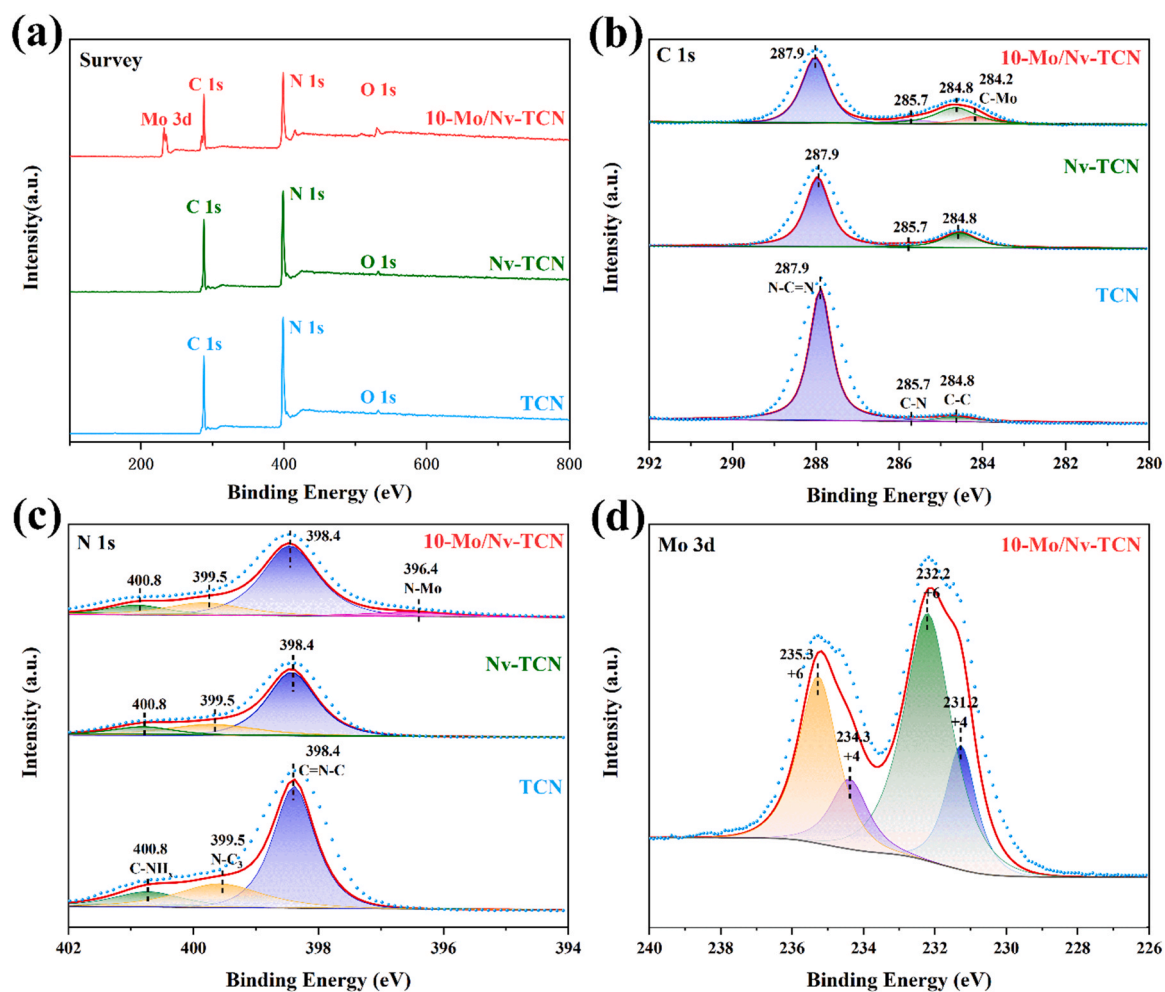


Fig. 4. XPS spectra for TCN, Nv-TCN, and 10-Mo/Nv-TCN: a) survey spectra, b) C1s, c) N1s, and d) Mo3d.

bond, respectively [68,69]. By comparison with Fig. 4b, TCN and Nv-TCN do not generate new peaks, while the peak corresponding to N-C=N for Nv-TCN is weakened relative to TCN, which is due to the introduction of N vacancy leading to the deletion of this bond. For 10-Mo/Nv-TCN. A new peak belonging to C-Mo is formed at the 284.2 eV position [70], and it is believed that a strong electronic coupling has occurred between the atomic Mo and the g-C<sub>3</sub>N<sub>4</sub> support. Fig. S1c and Fig. 4c compare the high-resolution spectra of N1s element in different samples. The CN, TCN, and Nv-TCN show three obvious peaks, among which 398.4 eV represents sp<sup>2</sup> hybridized aromatic N,

399.5 eV represents N-C<sub>3</sub> group, and 400.8 eV corresponds to terminal C-NH<sub>2</sub> amino functions [71]. After the introduction of N defect, the peak strength of N1s in the Nv-TCN sample (especially C=N-C) is significantly weakened, suggesting that the N vacancy is indeed generated in the material. Furthermore, the peak at 396.4 eV in the spectrum of the 10-Mo/Nv-TCN sample reflects the formation of N-Mo [35]. The Mo 3d element peak is only observed in the 10-Mo/Nv-TCN sample. In Fig. 4d, The Mo 3d spectrum of 10-Mo/Nv-TCN can be separated into two pairs of peaks, where the two pairs of peaks at 231.2/234.3 and 232.2/235.3 eV correspond to Mo<sup>4+</sup> and Mo<sup>6+</sup>, of which Mo<sup>6+</sup> occupies

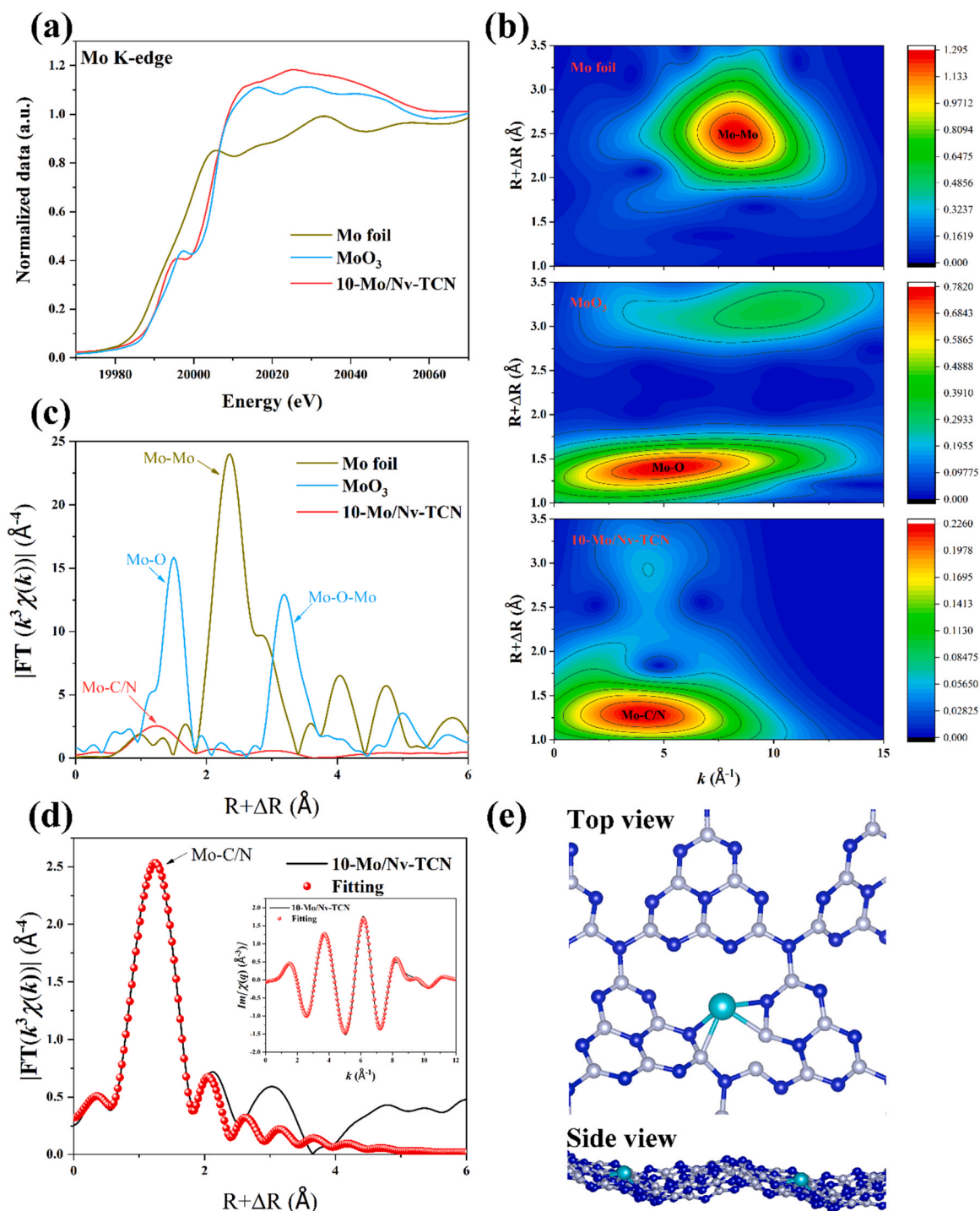
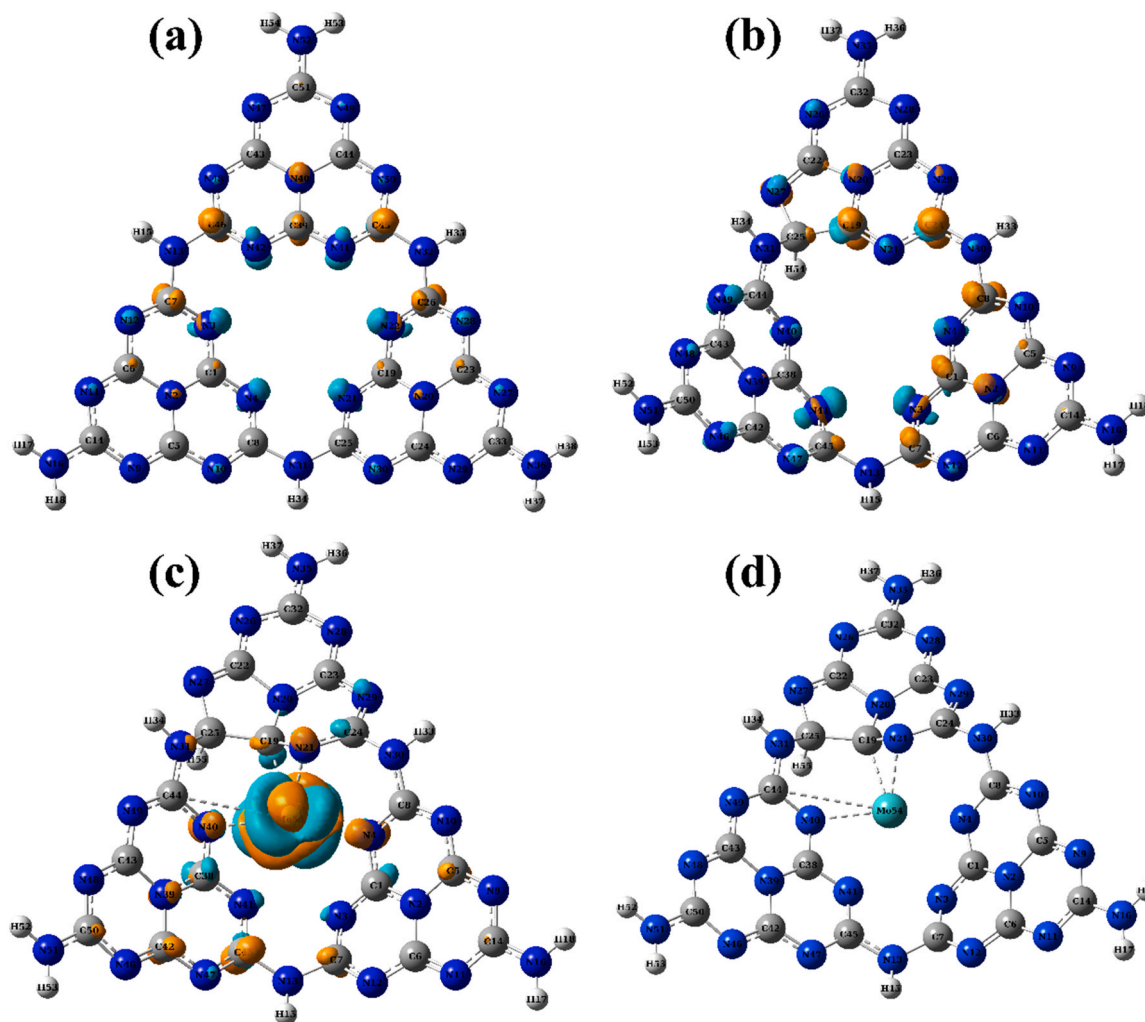


Fig. 5. a) XANES and c) FT-EXAFS spectra of Mo foil, MoO<sub>3</sub>, and 10-Mo/Nv-TCN at Mo K-edge. b) WT-EXAFS spectra of Mo foil, MoO<sub>3</sub>, and 10-Mo/Nv-TCN. d) FT-EXAFS fitting curves of the 10-Mo/Nv-TCN at Mo K-edge, inset: q space fitting curves of the 10-Mo/Nv-TCN. e) Optimized DFT calculation model of 10-Mo/Nv-TCN (gray, carbon; blue, nitrogen; turquoise, molybdenum).

the majority [70]. In conclusion, the results of XPS analysis on the one hand confirmed that there are a certain number of N vacancies in the material, and on the other hand, it also indicated that a stable coordination structure was formed between Mo atom and Nv-TCN, and the strong interaction was mainly caused by the Mo-C/N bond.

To further explore the chemical states and local coordination environment of Mo species at the atomic level, synchrotron radiation-based XANES and EXAFS characterizations at Mo K-edge were performed. As shown in XANES curves in Fig. 5a, the position of 10-Mo/Nv-TCN curve shifts significantly in the direction of higher energy compared with that of Mo foil, indicating that Mo species have a positive valence state. In addition, the absorption edge of the sample is close to  $\text{MoO}_3$ , which proves that Mo atoms exist mainly in the form of +6 valence. The edge front of the sample near 19995 eV moves forward relative to  $\text{MoO}_3$ , which is the result of interaction between Mo species and coordination atoms (such as C or N) with less electronegativity than O. The wavelet transform (WT) spectra in Fig. 5b can reflect the distance of coordination atoms and distinguish the types of coordination atoms [72]. The k value corresponding to the contour center of 10-Mo/Nv-TCN sample is less than Mo foil and  $\text{MoO}_3$ , which means that there is almost no Mo-Mo coordination in the sample, but coordination occurs with non-metallic atoms whose mass number is less than O. In Fig. 5c, Fourier transform (FT)-EXAFS exhibits that the 10-Mo/Nv-TCN sample appears a single peak at about 1.3 Å, which is caused by Mo-C or Mo-N bonds [73]. For Mo foil, the Mo-Mo signal is concentrated at 2.6 Å, while the

10-Mo/Nv-TCN sample has almost no obvious peak at this position. This result once again proves that the Mo species is dispersed in the form of single atoms on the Nv-TCN surface. Quantitative structural parameters of Mo species in different samples are displayed in Fig. 5d, Fig. S2, and Table S1. These results can explain the Mo-C/N coordination structure formed by the Mo atom and the support in the 10-Mo/Nv-TCN sample, and the number of coordination was quantized to be about 3.9. In addition to sample characterization techniques, theoretical calculation methods are also used to further explore the local coordination environment of Mo atoms. The Mo/Nv-TCN structure was optimized by DFT to obtain the most thermodynamically stable model. Meanwhile, the adsorption energy of the coordination structure was calculated. As shown in Fig. 5e, the single-atom Mo is located in the interlayer of Nv-TCN, and is connected with Nv-TCN support by two Mo-C and two Mo-N bonds to form a Mo-2 C/2 N coordination structure. This coordination model is consistent with the results of EXAFS both in terms of the species and number of coordination atoms. According to the energy of Mo/Nv-TCN (-947.57 eV), Nv-TCN (-940.66 eV), and Mo (-0.23 eV), the adsorption energy of Mo-2 C/2 N structure is finally calculated as -6.68 eV, which proves the stability of the structure. As for the formation mechanism of single atom Mo, on the one hand, under high temperature and high pressure, the N vacancies in the material can anchor Mo atoms, thus causing Mo atoms to bond with Nv-TCN molecules at specific sites; on the other hand, solvothermal reaction ensures the uniform dispersion of Mo atoms and further inhibits the aggregation



**Fig. 6.** Fukui function CDD of a) TCN, b) Nv-TCN, and c) Mo/Nv-TCN (The orange and turquoise colors represent the positive and negative phases of the molecular orbital). d) The chemical structure of Mo/Nv-TCN (gray, carbon; blue, nitrogen; white, hydrogen; turquoise, molybdenum).

of atoms. The combination of these factors leads to the successful formation of single atom Mo.

In order to further analyze the changes in electronic structure of TCN caused by N vacancy and atomic Mo, and to determine the transfer trend of photogenerated electrons and the active site, the local structural units of tri-s-triazine ring in CN molecules were analyzed by Fukui function [57]. By adding and subtracting electrons ( $q(N+1)$  or  $q(N-1)$ ) into the structural units of CN, the electron gain and loss capacities of different atoms in the material molecules is calculated theoretically [74], and then the internal charge transfer situation is simulated. Fig. S3 specifically lists the Fukui index isosurfaces of TCN, Nv-TCN and Mo/Nv-TCN. In addition, the Fukui function condensed dual descriptors (CDD) isosurfaces of TCN, Nv-TCN and Mo/Nv-TCN are compared (Fig. 6). It can be seen that compared with TCN, the introduction of N vacancy weakens the conjugation effect of triazine ring elements, destroys the delocalized  $\pi$  bond, and leads to the uneven distribution of charge. When the atomic Mo is introduced, the charge distribution of Nv-TCN changes again. Mo atoms are closely surrounded by the Fukui index isosurface, which proves that the surface charge changes of Mo atoms are the most significant. The specific value can be obtained from Table S2. Among all the analyzed atoms, the absolute value of CDD of Mo atom (0.0789) is the largest. In the photocatalytic system, the  $f$  is used to measure the electron loss ability of different atoms, and then the electron distribution of atoms inside the material during the photocatalytic reaction is simulated. The Mo atom displays a higher  $f$  value (0.1591), indicating that Mo atoms acted as the main active site. At the same time, there is a

tendency of electron transfer from surrounding atoms to Mo atoms. Therefore, the introduction of atomic Mo leads to the directional transfer of local charge on the surface of Nv-TCN, and the Mo-2 C/2 N bonds function as the bridge of charge transfer.

### 3.2. Optical property

To measure the light absorption performance of the sample and explore its band structure, the UV-vis DRS is shown in Fig. 7a. Typically, CN has a steep semiconductor absorption edge at 450 nm. Compared with bulk CN, the absorption edge of TCN and Nv-TCN is redshifted, which is closely related to defect effect and the light reflection effect of the tubular structure. For the sample with higher Mo atom content, the redshift of absorption edge is more obvious, and the light absorption performance of the material gradually becomes stronger. This indicates that the introduction of single atom Mo helps to enhance the visible light absorption capacity of the material. The Kubelka-Munk function was used to convert the data of UV-vis DRS to obtain the bandgap energy of the photocatalyst, as shown in Fig. 7b. The bandgaps of CN, TCN, Nv-TCN, and 10-Mo/Nv-TCN are 2.56, 2.48, 2.41, and 2.33 eV, respectively, showing a trend of gradually narrowing. To further clarify the band structure of the samples, the valence band (VB) potentials of CN, TCN, Nv-TCN, and 10-Mo/Nv-TCN were 1.81, 1.74, 1.71, and 1.66 eV, which were reflected by the XPS valence band spectrum (Fig. 7c). The conduction band (CB) potential of the sample can be calculated according to the Eq. (4):

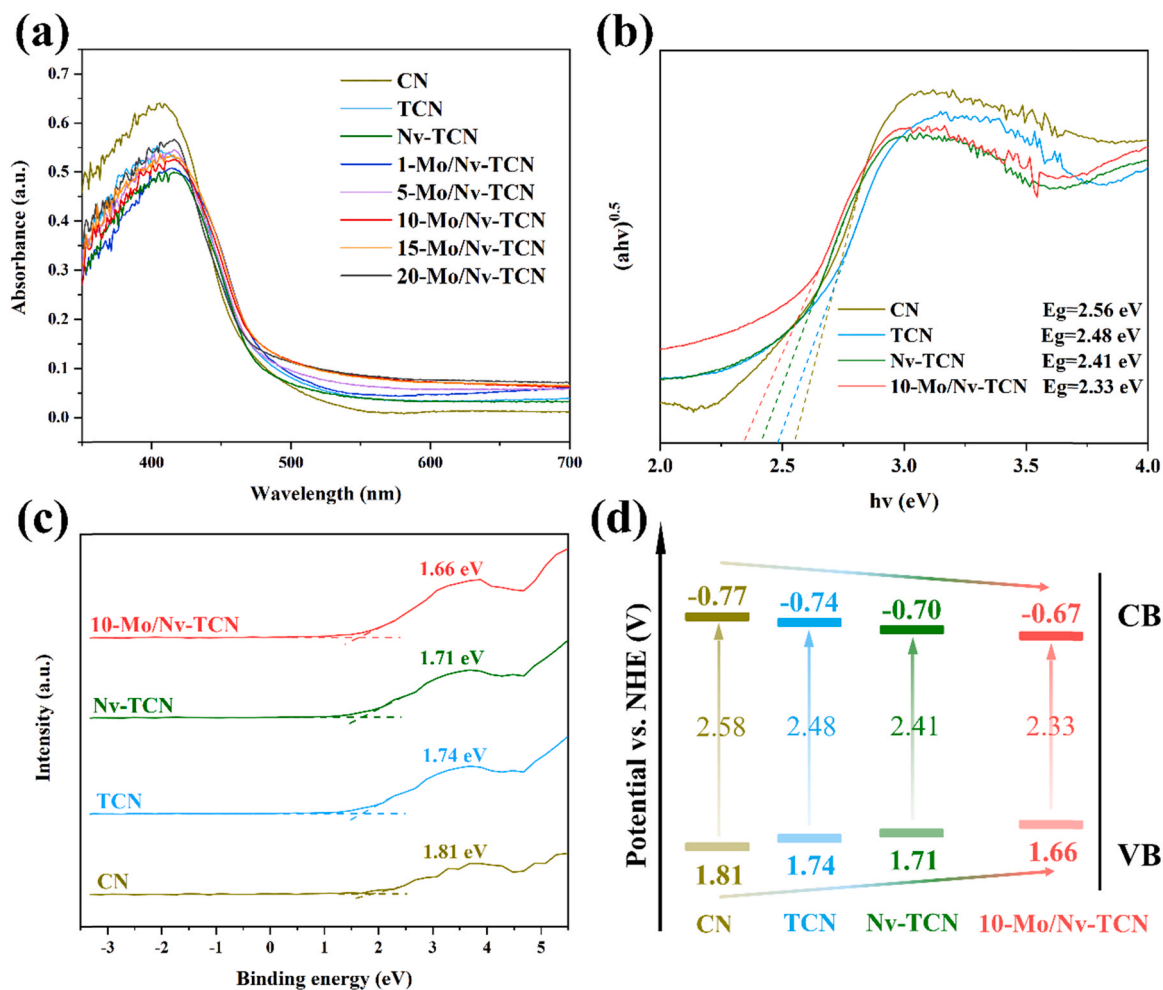


Fig. 7. a) UV-vis DRS and b) corresponding plots of transformed Kubelka-Munk function versus photon energy of the samples, c) VB-XPS spectra and d) the estimated band structure alignments of the samples.

$$E_{CB} = E_{VB} - E_g \quad (4)$$

Where  $E_g$  represents the band gap energy, and  $E_{CB}$  and  $E_{VB}$  represent the potential of CB and VB, respectively. According to these results, the band structure diagrams of different samples were drawn in Fig. 7d. In the process of gradual modification of the material, the band structure of the sample was also constantly changing. For TCN, the change of morphology and the difference of precursors are the reasons for its narrow band gap compared with CN [8]. When N vacancies are introduced, the absence of N atoms in the  $\pi$ -conjugated aromatic ring leads to the reconstruction of the band structure, and relevant studies have shown that a new midgap states will appear [47]. Generally speaking, for the doping of metal elements, in addition to the partial lattice distortion of the original chemical structure, the impurity level is an important factor leading to the change of the band structure. In this study, the appearance of Mo 4d orbital induced the band structure to change again [37].

To investigate the electron and hole behavior of the photocatalytic process, PL and TRPL were used to characterize the separation and transfer properties of the charge carriers. From Fig. 8a, under the excitation condition of 340 nm wavelength, CN shows the PL curve of maximum density. The curve densities of TCN and Nv-TCN gradually weaken. After Mo is loaded on Nv-TCN, PL density decreases again, and the signal of 10-Mo/Nv-TCN is the weakest. Therefore, the morphology modification of CN and the introduction of defects can inhibit the recombination of photogenerated charges, while the loading of single atom Mo further promotes the separation of charge carriers and has a lower charge recombination rate. In Fig. 8b, the lifetimes of photogenerated electrons produced by different samples is measured by TRPL decay curve. Fig. 8c lists the average electron lifetimes ( $\tau_{ave}$ ) after calculation, and the detailed calculation method is shown in the following Eq. (5):

$$\tau_{ave} = \frac{B_1 \tau_1^2 + B_2 \tau_2^2}{B_1 \tau_1 + B_2 \tau_2} \quad (5)$$

Among them,  $\tau_1$  and  $\tau_2$  respectively represent two different lifetime components, while  $B_1$  and  $B_2$  represent their corresponding normalized amplitudes [75]. It can be seen from the calculation results that the fluorescence lifetime of TCN is 7.78 ns, which is greater than the 6.45 ns

of bulk CN. This phenomenon is caused by the morphology of the sample and is related to its specific surface area, which inhibits the recombination of electrons and holes. N vacancies can be used as electron capture sites [76], thereby promoting electrons to participate in a series of activation reactions and shortening the electron lifetime (6.89 ns). The 10-Mo/Nv-TCN sample exhibits the shorter electron fluorescence lifetime (6.50 ns), indicating that single atom Mo can enhance separation and transfer capabilities of charge carriers.

Fig. 8d shows the Mott-Schottky curves of different samples. First of all, the curves of all samples show a positive slope, indicating that they belong to n-type semiconductor materials. In addition, the charge carrier density ( $N_D$ ) generated by each sample can be compared through the slope of the curve. The specific calculation method is shown in the following Eq. (6) [77]:

$$N_D = \frac{2}{q\epsilon\epsilon_0} \frac{1}{\text{slope}} \quad (6)$$

Among them,  $q$  ( $1.602 \times 10^{-19}$  C),  $\epsilon$  (5.25), and  $\epsilon_0$  ( $8.85 \times 10^{-14}$  F cm $^{-2}$ ) are all constants:  $q$  represents the electronic charge;  $\epsilon$  and  $\epsilon_0$  represent the dielectric constant of g-C $_3$ N $_4$  and the permittivity in vacuum, respectively. Therefore, the density of charge carriers is inversely proportional to the slope of the sample's Mott-Schottky curve. The charge carrier densities of the four samples were sorted as follows: 10-Mo/Nv-TCN > Nv-TCN > TCN > CN.

In addition, the photo-electrochemical test of the samples was also used to evaluate their photogenerated charge carrier behavior. The EIS curve in Fig. 8e reflects the electrical conductivity of the sample. TCN and Nv-TCN show a smaller slope than bulk CN, while 10-Mo/Nv-TCN has the smallest arc. So, the electrical resistance of the sample is CN > TCN > Nv-TCN > 10-Mo/Nv-TCN, while the electrical conductivity is just the opposite. The better electrical conductivity endows the samples with stronger electron transfer performance. In Fig. 8f, transient photocurrent responses curves reflect the ability of different photocatalysts to excite electrons and holes. In this experiment, the time interval between the light source on and off is 10 s. When the light is turned on, all the samples show obvious photocurrent signals, which basically remain unchanged until they drop to the background value at the moment of the next light off. The sample with the strongest photocurrent density is 10-Mo/Nv-TCN, followed by Nv-TCN and TCN, while

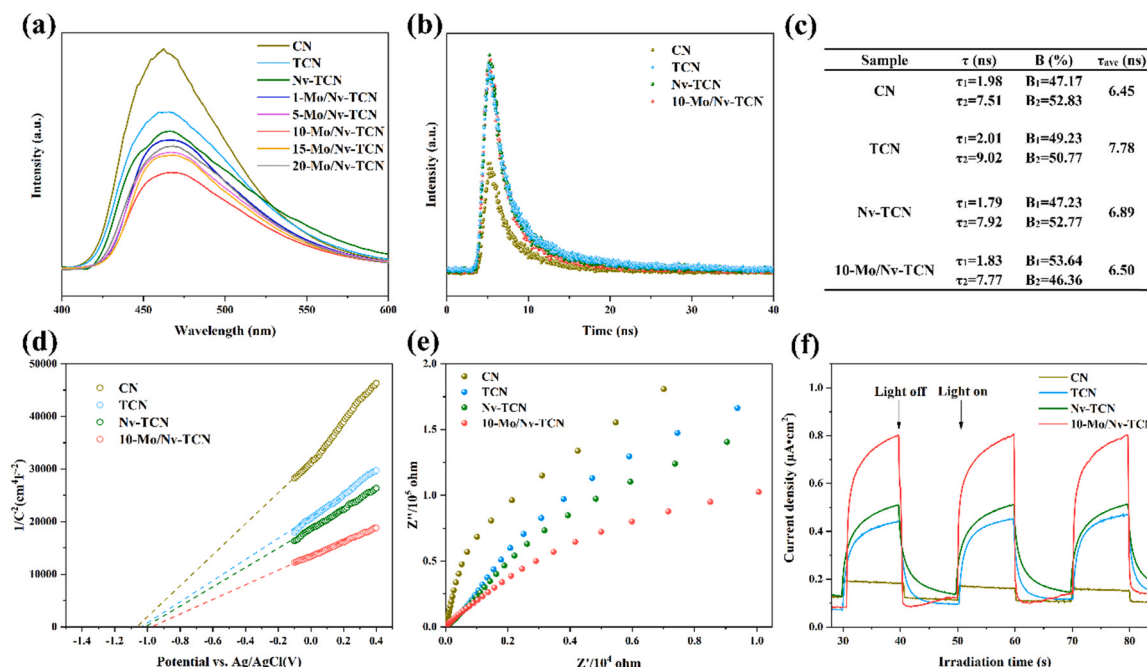


Fig. 8. a) Steady-state PL spectra, b) TRPL decay spectra, c) TRPL lifetimes, d) Mott-Schottky plot, e) EIS, f) transient photocurrent curves of the samples.

bulk CN has the weakest signal. To sum up, these results all prove that, with the dual assistance of morphology and defect engineering, the implantation of single atom Mo can significantly enhance the excitation of photogenerated electrons, promote the separation and transfer of charge carriers, thus achieving more efficient photocatalytic performance.

### 3.3. Photocatalytic activities and mechanisms

In this study, TC was used as the removal object to measure the adsorption and photocatalytic capacity of different prepared photocatalysts. In Fig. 9a, the control curve reflects the change of TC concentration in the catalyst-free system, which indicated that TC has high stability and its self-decomposition can be ignored. All photocatalytic systems first undergo a 1 h dark reaction to evaluate the adsorption effect of the sample. There are different kinds of interactions between TC molecules and photocatalyst samples. First of all, the surface of TC molecule and Mo/Nv-TCN sample have different surface charge properties, and this characteristic will change with the pH of the solution, so there is electrostatic interaction between them [78]. Then, the saturated N in the chemical structure of Mo/Nv-TCN has exposed lone pairs of electrons, which will form hydrogen bonds with H-containing structures in the TC molecule, such as phenolic hydroxyl groups, terminal amino groups, and other hydroxyl groups. In addition, the  $\pi$ - $\pi$  stacking between the TC molecules and the photocatalyst sample is also a very important factor in the formation of adsorption [79]. Ultimately, the metallic Mo contained in Mo/Nv-TCN may have surface complexation with the polar

functional groups of TC molecules. It is these interactions that lead to the adsorption behavior of TC molecules on the surface of Mo/ Nv-TCN samples [80]. The adsorption effect of TCN and Nv-TCN on TC is slightly improved compared with that of bulk CN, which is caused by the increase of specific surface area of tubular morphology. The adsorption amount of TC gradually increased with the increase of Mo content in the sample, indicating that the single atom Mo is beneficial to the adsorption of TC, thereby promoting the degradation of TC. As a transition metal element, Mo is incorporated into the chemical structure of Nv-TCN, which will enhance the electropositivity of the sample surface and provide valence electrons [81]. Due to the large number of positively charged sites introduced by Mo atoms on the surface of the material, it will interact with negatively charged TC species, thereby promoting the adsorption performance of TC molecules. In addition, the exposed Mo on the surface may have a complexation with the polar functional groups of TC molecules to produce stronger adsorption capacity [80]. In the subsequent 1 h photocatalytic reaction, bulk CN showed the worst degradation efficiency (46.62%). The degradation performance can be optimized to a certain extent through morphology modification and N defect engineering, and the degradation efficiency is increased to 62.23% and 64.59%, respectively. However, it should be noted that in all catalytic systems, the high degradation ability of TC is largely dependent on the loading of single atom Mo. The TC removal efficiency of all the atomic Mo composite systems is better than that of the monomer CN system. At first, the photodegradation performance of the samples gradually enhanced with the increase of Mo content. The optimal 10-Mo/Nv-TCN composite sample shows the highest

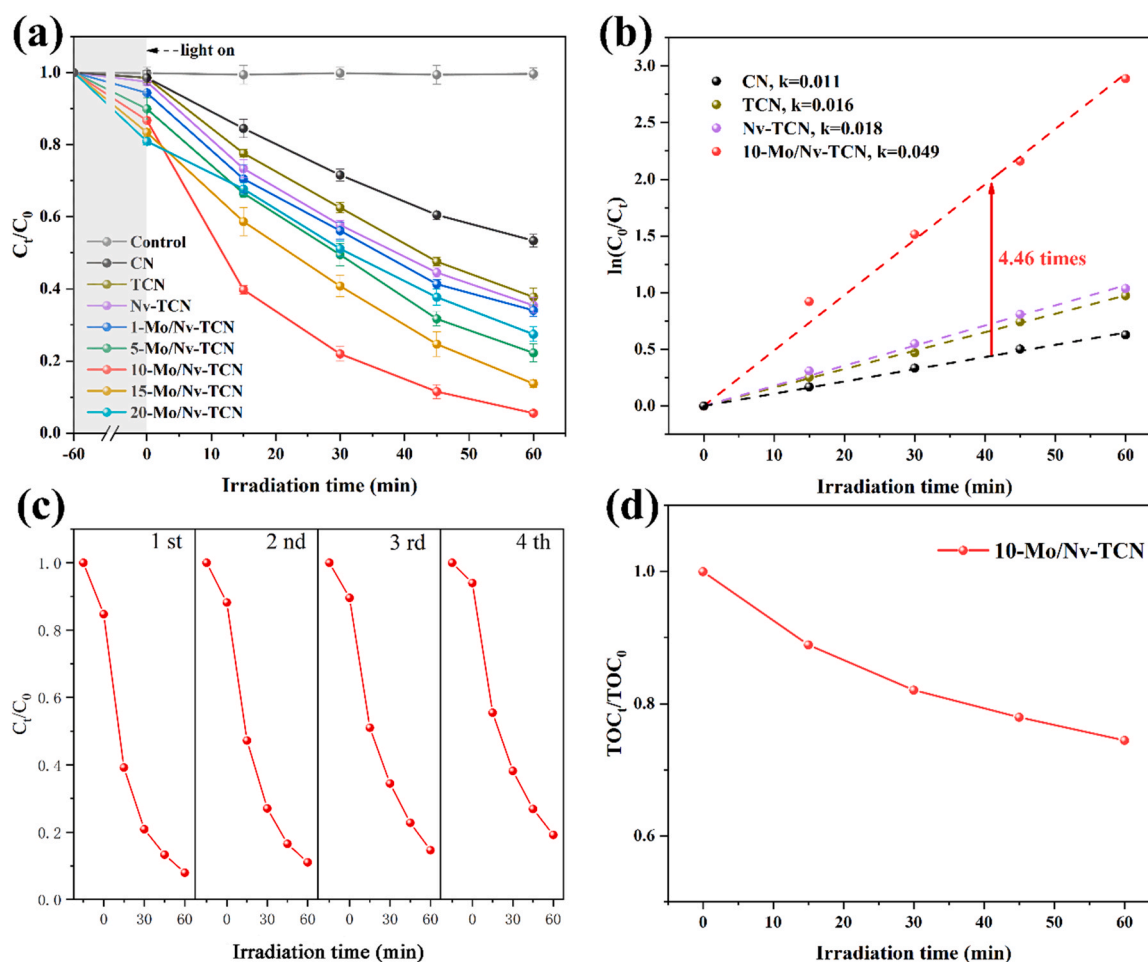


**Fig. 9.** a) Photocatalytic degradation efficiency and b) corresponding kinetic curves of TC with time over various samples under visible light irradiation. c) The cycling experiment for the degradation of TC by 10-Mo/Nv-TCN. d) TOC removal curves of TC on 10-Mo/Nv-TCN.

degradation efficiency of TC, which could reach 94.45%, under 1 h visible light illumination. Nevertheless, With the further increase of Mo content from 10-Mo/Nv-TCN to 20-Mo/Nv-TCN, the photocatalytic efficiency decreases obviously. This is due to the excessive atom load on the surface of the material, which affects the absorption of visible light. In addition, lots of Mo atoms may aggregate on the surface of the support, and the nanoparticles or clusters formed may become new recombination centers, resulting in the recombination of charge carriers [82]. The apparent rate constant ( $k$ ) of photocatalysis shown in Fig. 9b reflects the reaction kinetics of degradation, and the  $k$  was calculated by Eq. (7):

$$k = \frac{\ln(C_0/C_t)}{t} \quad (7)$$

The 10-Mo/Nv-TCN sample has the largest apparent rate constant ( $k = 0.049$ ), which is 4.46 times that of bulk CN. The reason for this phenomenon is partly due to the modification of morphology and defects, and mainly due to the promoting effect of single atom Mo loading. Meanwhile, 10-Mo/Nv-TCN sample and other  $g\text{-C}_3\text{N}_4$  based photocatalysts were compared for TC degradation ability (Table S3). Both the removal rate of TC and the apparent rate constant prove that 10-Mo/Nv-

TCN is a high-performance photocatalytic material.

To evaluate the stability of the sample, a cycle experiment was carried out on the 10-Mo/Nv-TCN sample. As shown in Fig. 9c, after each cycle, the photodegradation performance of the material is reduced to a certain extent. However, after four cycles of experiments, the degradation efficiency of TC can still maintain more than 75%, which proves that the sample has good reusability. In addition, the used 10-Mo/Nv-TCN samples were characterized by XPS, XRD, and FT-IR (Fig. S4). It was found that the chemical composition and structure of the material did not change significantly after photocatalytic degradation of TC, which further demonstrated its chemical stability. Meanwhile, the 10-Mo/Nv-TCN sample still basically maintained the previous tubular morphology after the reaction (Fig. S5), proving that the material has good morphological stability. The removal efficiency of TOC is used as an evaluation index to measure the mineralization performance of the photocatalyst on organic pollutants. As exhibited in Fig. 9d, the 10-Mo/Nv-TCN sample has a TOC removal efficiency of 25.6% after being excited by visible light for 60 min, which has certain mineralization properties.

In the process of TC degradation, a variety of intermediates will be produced. Using the LC-MS/MS technology to reasonably analyze the

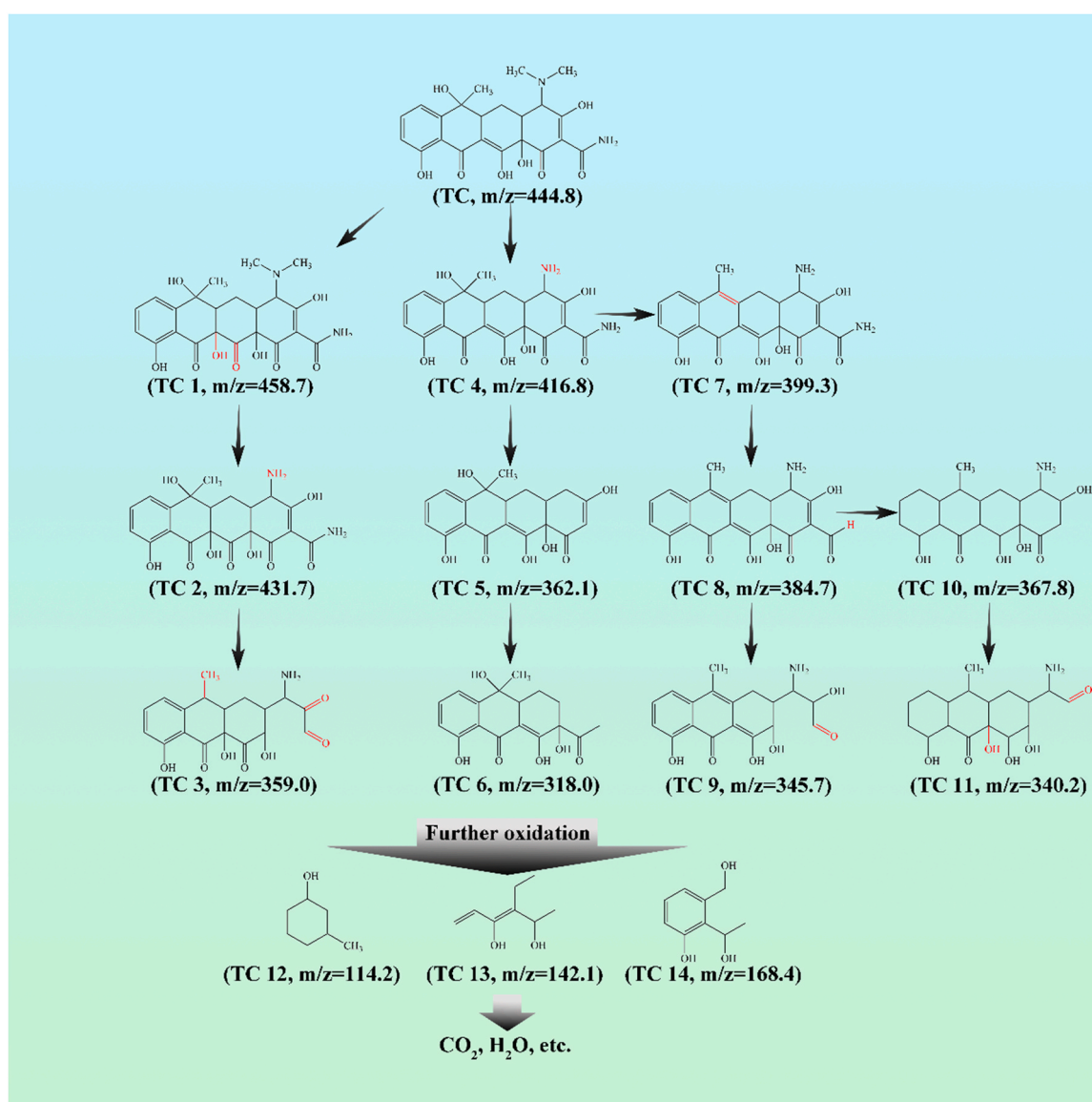


Fig. 10. Possible TC photodegradation pathway over 10-Mo/Nv-TCN.

intermediates is helpful to better clarify the degradation pathways of TC. Fig. S6 and Table S4 lists the intermediates that may be produced during the degradation process, including their  $m/z$ , molecular formula, and structure. The specific degradation pathway is shown in the Fig. 10. TC with 444.8  $m/z$  is first attacked by  $\bullet\text{OH}$  and then hydroxylated to form TC 1 ( $m/z = 458.7$ ). TC 2 ( $m/z = 431.7$ ) is produced by the loss of two N-methyl groups from TC 1. Following by, TC 2 is converted into TC 3 ( $m/z = 359.0$ ) by removing water molecules and ring-opening process. In another possible path, TC first loses two N-methyl groups to form TC 4 ( $m/z = 416.8$ ). TC 5 ( $m/z = 362.1$ ) is formed through deamidation and

deamidation. TC 6 ( $m/z = 318.0$ ) is produced through further dehydroxylation and ring-opening reaction. In addition, TC 4 can also be dehydrated to form TC 7 ( $m/z = 399.3$ ), which will undergo deamidation reaction in the next step to transform into TC 8 ( $m/z = 384.7$ ), followed by the cleavage of carboatomic ring to yield TC 9 ( $m/z = 345.7$ ). What's more, TC 8 can also undergo dealdehyde and multiple hydrogenation to form TC 10 ( $m/z = 367.8$ ). The cleavage of carboatomic ring and hydroxylation is assumed to occur on TC 10, as a result of generating TC 11 ( $m/z = 340.2$ ). Afterwards, these intermediates can be further decomposed into TC 12 ( $m/z = 114.2$ ), TC 13

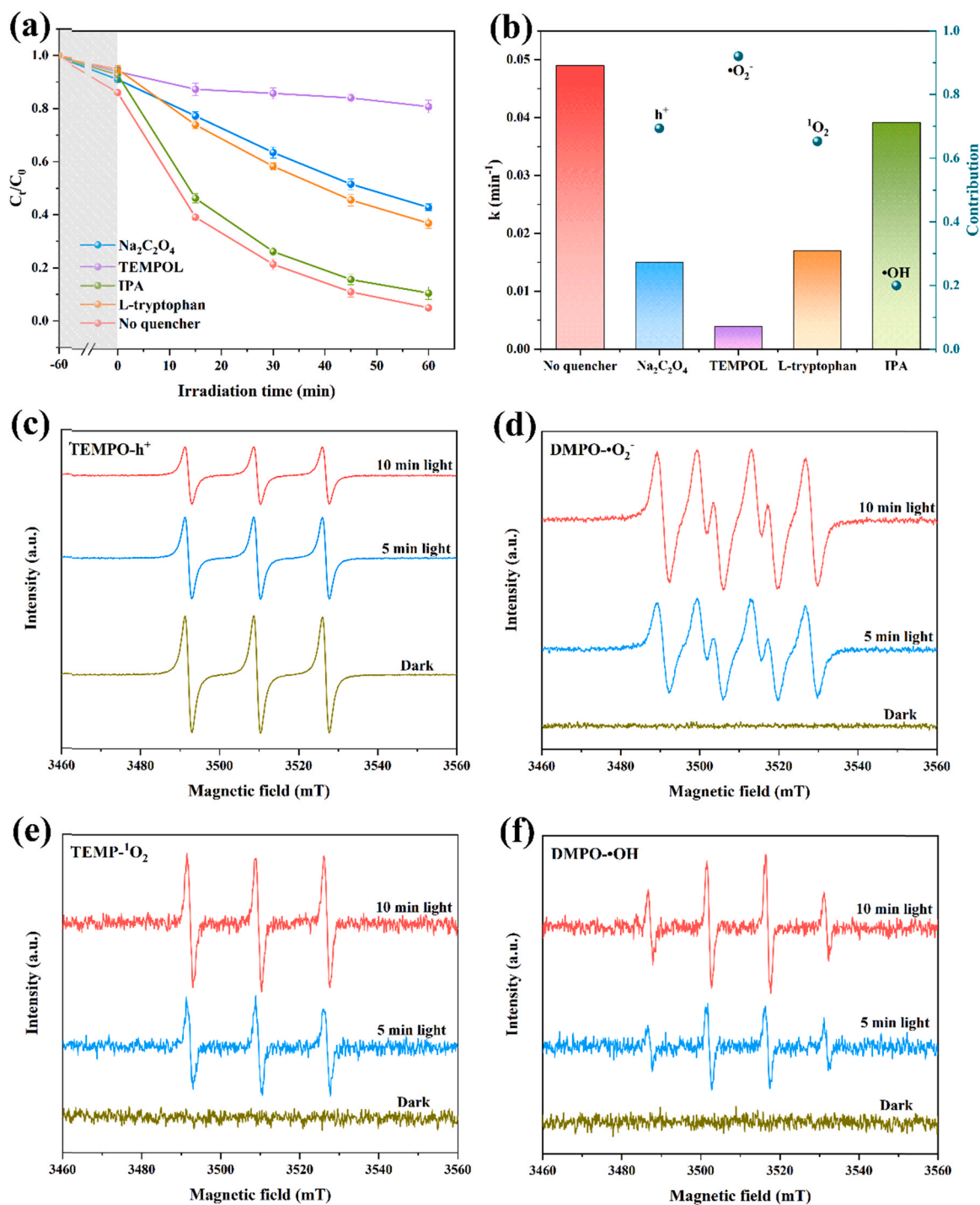


Fig. 11. a) Photocatalytic degradation curves of TC with different quenchers over 10-Mo/Nv-TCN under visible light irradiation and b) the corresponding kinetic constants as well as the relative contributions of different quenchers. ESR spectra of reactive species tapped by the c) TEMPO- $\text{h}^+$  adducts, d) DMPO- $\bullet\text{O}_2^-$  adducts, e) TEMP- $^1\text{O}_2$  adducts, and f) DMPO- $\bullet\text{OH}$  adducts for 10-Mo/Nv-TCN under visible light irradiation.

( $m/z = 142.1$ ), and TC 14 ( $m/z = 168.4$ ) with lower molecular weights. Finally, after further mineralization, these small molecules can be completely converted into  $\text{CO}_2$ ,  $\text{H}_2\text{O}$ , or other molecules.

To further clarify the degradation process, Fukui function based on DFT is used to determine the reactive sites of TC molecules [83]. In this analysis, CDD values is mainly used to measure the reactivity of different sites. Generally speaking, sites with higher CDD absolute values are more vulnerable to attack [74]. As shown in Fig. S7 and Table S5, the N45 atom shows a relatively low CDD value ( $-0.0364$ ) and is clearly surrounded by the isosurface of Fukui index, suggesting that it is a critical site for reactive species. Moreover, the  $f^0$  value (0.0304) and  $f^0$  isosurface of N45 atoms also reflect their tendency to be attacked by free radicals. This result is consistent with the loss of the two N-methyl groups in the above pathway analysis, and is a core step in the overall pathway. Besides, through comparative analysis, C20 (0.0942), C22 (0.0850), O23 (0.0791), and O38 (0.0538) all have high CDD absolute values, which is closely related to subsequent processes such as ring opening and dehydration. The results of these theoretical calculations can effectively support the inferred results of the TC molecular degradation pathways.

For the purpose of understanding the contribution of reactive species generated by the 10-Mo/Nv-TCN sample in the process of photocatalytic degradation of TC, the trapping experiment was used to deeply explore the degradation mechanism. In this work, 10 mM  $\text{Na}_2\text{C}_2\text{O}_4$ , TEMPOL, L-tryptophan, and IPA were used as quenchers for holes ( $\text{h}^+$ ), superoxide radical ( $\bullet\text{O}_2^-$ ), singlet oxygen ( $^1\text{O}_2$ ), and hydroxyl radicals ( $\bullet\text{OH}$ ), respectively. As displayed in Fig. 11a, after the quenching of  $\bullet\text{O}_2^-$  by TEMPOL, the degradation efficiency of TC decreased significantly from 94.5% to 18.5%. When  $\text{Na}_2\text{C}_2\text{O}_4$ , L-tryptophan, and IPA were present in the photocatalytic system, the degradation efficiency decreased to 56.5%, 62.56%, and 88.91%, respectively. Fig. 11b shows the kinetic constants and corresponding contributions under different quencher conditions. The apparent rate constants in the presence of  $\text{Na}_2\text{C}_2\text{O}_4$ , TEMPOL, L-tryptophan, and IPA were 0.015, 0.0039, 0.017, and  $0.039 \text{ min}^{-1}$ , respectively. The contribution of each active species was calculated according to the Eqs. (8)–(11):

$$R_{\text{h}^+} \approx \frac{(k - k_{\text{Na}_2\text{C}_2\text{O}_4})}{k} \quad (8)$$

$$R_{\bullet\text{O}_2^-} \approx \frac{(k - k_{\text{TEMPOL}})}{k} \quad (9)$$

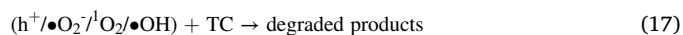
$$R_{^1\text{O}_2} \approx \frac{(k - k_{\text{L-tryptophan}})}{k} \quad (10)$$

$$R_{\bullet\text{OH}} \approx \frac{(k - k_{\text{IPA}})}{k} \quad (11)$$

According to the above formula, the contribution of  $\text{h}^+$ ,  $\bullet\text{O}_2^-$ ,  $^1\text{O}_2$ , and  $\bullet\text{OH}$  to TC degradation was 69.4%, 92.0%, 65.3%, and 20.0%, respectively. It is worth noting that the total contribution of the different active species is significantly more than 100%, mainly due to the very complex radical chemistry involved in the photocatalytic reaction [84]. Under certain conditions, there exists transformation relationship between different active species. Therefore, in addition to quenching a specific active species, a trapping agent can also affect a series of subsequent transformation processes, resulting in a phenomenon of over 100% contribution [85]. In summary, the most important active species produced by 10-Mo/Nv-TCN photocatalyst during the degradation of TC was  $\bullet\text{O}_2^-$ , followed by  $\text{h}^+$ ,  $^1\text{O}_2$ , and  $\bullet\text{OH}$ . In addition, 5,5-dimethyl-1-pyrroline N-oxide (DMPO), the 2,2,6,6-tetramethylpiperidine-1-oxyl (TEMPO), and 2,2,6,6-tetramethylpiperidine (TEMP) spin-trapping ESR technology was used to monitor the production of active species over the 10-Mo/Nv-TCN more intuitively. As shown in Fig. 11c, TEMPO- $\text{h}^+$  adduct generates a signal with the peak density of 1:1:1, which proves the generation of photogenerated  $\text{h}^+$ . The peak density is

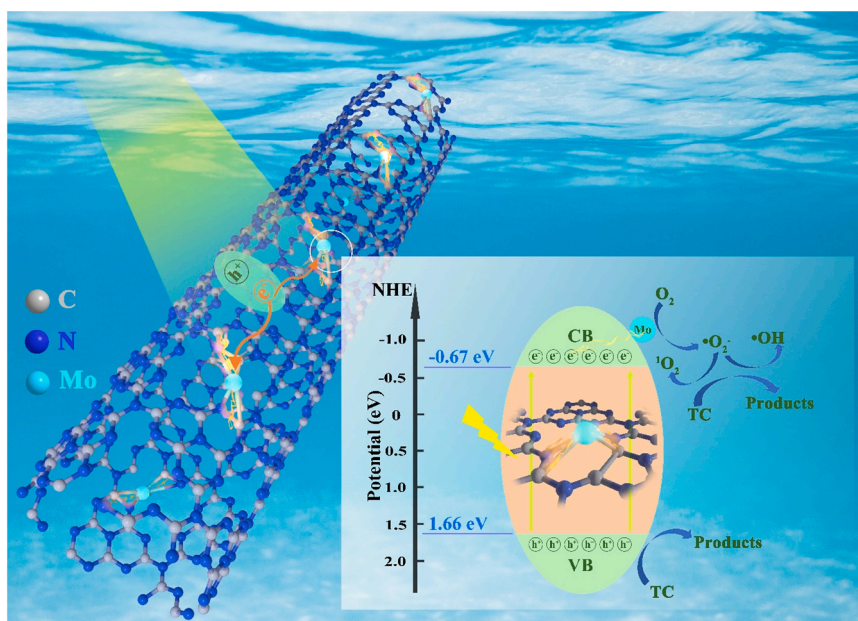
the highest in the dark condition, and decreases gradually with the prolonging of irradiation time. Similarly, the 1:2:2:1, 1:1:1:1, and 1:1:1 density signal shown in Figs. 11d, 11e, and 11f correspond to DMPO- $\bullet\text{O}_2^-$ , TEMP- $^1\text{O}_2$ , and DMPO- $\bullet\text{OH}$ , respectively [86]. Under dark conditions, none of these three kinds of signals are produced, but with the beginning of light excitation, these three kinds of signal curves begin to appear and the density gradually strengthens over time. Therefore, the ESR curve further confirms the generation of active species during the photocatalytic degradation, and it continues to generate with the extension of illumination time.

A possible photocatalytic degradation mechanism of TC over 10-Mo/Nv-TCN was delineated in Scheme 2. Under visible light irradiation, the photocatalyst produces photogenerated electrons and holes (Eq. (12)). Due to the effect of loading single atoms, the local photogenerated charge carriers have a tendency to migrate to Mo atom, and the Mo-2 C/2 N bond acts as the bridge of charge transfer, so the single atom Mo becomes the main active site of the reaction. The CB edge potential of 10-Mo/Nv-TCN ( $-0.67 \text{ V}$  vs. NHE) is more negative than the standard redox potential of  $\text{O}_2/\bullet\text{O}_2^-$  ( $-0.33 \text{ V}$  vs. NHE), which means that the electrons on CB can combine with molecular oxygen to produce  $\bullet\text{O}_2^-$  (Eq. (13)). The combination of  $\bullet\text{O}_2^-$  and  $\text{h}^+$  leads to the formation of  $^1\text{O}_2$  (Eq. (14)), and  $\bullet\text{O}_2^-$  can also react with electrons ( $\text{e}^-$ ) and  $\text{H}^+$  to form  $\text{H}_2\text{O}_2$  (Eq. (15)). In the subsequent reaction,  $\text{H}_2\text{O}_2$  will continue to combine with  $\text{e}^-$  to form  $\bullet\text{OH}$  (Eq. (16)). The  $\text{h}^+$ ,  $\bullet\text{O}_2^-$ ,  $^1\text{O}_2$ , and  $\bullet\text{OH}$  produced in the above process act as important active species and react with TC molecules to facilitate the degradation process (Eq. (17)).



#### 4. Conclusion

In summary, the isolated single atom Mo was incorporated into the Nv-TCN by a simple solvothermal method, and SACs were optimized by morphology modification and defect engineering of the support. The tubular morphology gives CN a larger specific surface area, thereby providing more single atom anchor sites. Based on the results of sample characterization and theoretical calculation, it is speculated that the existence of N vacancies induces the formation of stable Mo-2 C/2 N coordination between atomic Mo and Nv-TCN carrier. The Mo single atoms in the Nv-TCN expands the absorption range of visible light, accelerates the separation and transfer of photogenerated electrons, reduces the recombination rate of electron-hole pairs, and increases the charge density. The local charge on the surface of carbon nitride tends to transfer in a directional way, and the Mo-2 C/2 N bonds act as the bridge of charge transfer. At the same time, changes in the internal electronic structure cause Mo atoms to become the main reactive center. Benefiting from the cooperation of support modification and single atom Mo, the 10-Mo/Nv-TCN exhibits excellent photocatalytic performance toward TC degradation. As the optimal sample, the 10-Mo/Nv-TCN sample shows an excellent apparent rate constant ( $0.049 \text{ min}^{-1}$ ) for degradation of TC under visible light irradiation, which is 4.46 times that of pristine CN. This study sheds light on the rational manipulation of single atom incorporated modified photocatalysts for the high-performance degradation of antibiotics.



Scheme 2. The proposed photocatalytic degradation mechanism of TC in Mo/Nv-TCN.

### CRediT authorship contribution statement

**Chen Zhang:** Conceptualization, Supervision, Project administration, Funding acquisition, Writing-review & editing. **Deyu Qin:** Conceptualization, Formal analysis, Data curation, Methodology, Writing-original draft. **Yin Zhou:** Formal analysis, Supervision, Validation. **Fanzhi Qin:** Methodology, Software, Validation. **Hou Wang:** Supervision, Validation, Writing-review & editing. **Wenjun Wang:** Validation, Writing-review & editing. **Yang Yang:** Validation, Writing-review & editing. **Guangming Zeng:** Resources, Funding acquisition.

### Declaration of Competing Interest

The authors declare that they have no known competing financial interests or personal relationships that could have appeared to influence the work reported in this paper.

### Acknowledgements

This study was financially supported by the Program for the National Natural Science Foundation of China (52170162, 51809090, U20A20323, 51521006), the Hunan Youth Talents Support Program (2021RC3049), the Natural Science Foundation of Hunan Province, China (Grant No. 2019JJ50077), and the Fundamental Research Funds for the Central Universities (531118010114).

### Appendix A. Supporting information

Supplementary data associated with this article can be found in the online version at doi:10.1016/j.apcatb.2021.120904.

### References

- [1] H. Williams, Smith, Effect of prohibition of the use of tetracyclines in animal feeds on tetracycline resistance of faecal *e. coli* of pigs, *Nature* 243 (1973) 237–238.
- [2] R.L. McCorry, J.A. Weaver, TETRACYCLINE, *Lancet* 265 (1955) 1102–1105.
- [3] Y. Luo, L. Xu, M. Rysz, Y. Wang, H. Zhang, P.J.J. Alvarez, Occurrence and transport of tetracycline, sulfonamide, quinolone, and macrolide antibiotics in the Haihe river basin, China, *Environ. Sci. Technol.* 45 (2011) 1827–1833.
- [4] C. Huang, C. Zhang, D. Huang, D. Wang, S. Tian, R. Wang, Y. Yang, W. Wang, F. Qin, Influence of surface functionalities of pyrogenic carbonaceous materials on the generation of reactive species towards organic contaminants: A review, *Chem. Eng. J.* 404 (2021), 127066.
- [5] B. Wang, Y. Zhang, D. Zhu, H. Li, Assessment of bioavailability of biochar-sorbed tetracycline to *Escherichia coli* for activation of antibiotic resistance genes, *Environ. Sci. Technol.* 54 (2020) 12920–12928.
- [6] S. Tian, C. Zhang, D. Huang, R. Wang, G. Zeng, M. Yan, W. Xiong, C. Zhou, M. Cheng, W. Xue, Y. Yang, W. Wang, Recent progress in sustainable technologies for adsorptive and reactive removal of sulfonamides, *Chem. Eng. J.* 389 (2020), 123423.
- [7] C. Zhang, G. Zeng, D. Huang, C. Lai, M. Chen, M. Cheng, W. Tang, L. Tang, H. Dong, B. Huang, X. Tan, R. Wang, Biochar for environmental management: Mitigating greenhouse gas emissions, contaminant treatment, and potential negative impacts, *Chem. Eng. J.* 373 (2019) 902–922.
- [8] C. Zhang, Y. Zhou, W. Wang, Y. Yang, C. Zhou, L. Lei, D. He, H. Luo, D. Huang, Formation of Mo<sub>2</sub>C/hollow tubular g-C<sub>3</sub>N<sub>4</sub> hybrids with favorable charge transfer channels for excellent visible-light-photocatalytic performance, *Appl. Surf. Sci.* 527 (2020), 146757.
- [9] Y. Yang, X. Li, C. Zhou, W. Xiong, G. Zeng, D. Huang, C. Zhang, W. Wang, B. Song, X. Tang, X. Li, H. Guo, Recent advances in application of graphitic carbon nitride-based catalysts for degrading organic contaminants in water through advanced oxidation processes beyond photocatalysis: A critical review, *Water Res.* 184 (2020), 116200.
- [10] H. Tan, J. Li, M. He, J. Li, D. Zhi, F. Qin, C. Zhang, Global evolution of research on green energy and environmental technologies: A bibliometric study, *J. Environ. Manag.* 297 (2021), 113382.
- [11] Q. Sun, N. Wang, J. Yu, J.C. Yu, A hollow porous CdS photocatalyst, *Adv. Mater.* 30 (2018), 1804368.
- [12] M. Nolan, A. Iwaszuk, A.K. Lucid, J.J. Carey, M. Fronzi, Design of novel visible light active photocatalyst materials: surface modified TiO<sub>2</sub>, *Adv. Mater.* 28 (2016) 5425–5446.
- [13] X. Li, W. He, C. Li, B. Song, S. Liu, Synergetic surface modulation of ZnO/Pt@ZIF-8 hybrid nanorods for enhanced photocatalytic CO<sub>2</sub> valorization, *Appl. Catal. B* 287 (2021), 119934.
- [14] Z. Pan, G. Zhang, X. Wang, Polymeric carbon nitride/reduced graphene oxide/Fe<sub>2</sub>O<sub>3</sub>: all-solid-state Z-scheme system for photocatalytic overall water splitting, *Angew. Chem. Int. Ed.* 58 (2019) 7102–7106.
- [15] S. Chen, D. Huang, G. Zeng, W. Xue, L. Lei, P. Xu, R. Deng, J. Li, M. Cheng, In-situ synthesis of facet-dependent BiVO<sub>4</sub>/Ag<sub>3</sub>PO<sub>4</sub>/PANI photocatalyst with enhanced visible-light-induced photocatalytic degradation performance: Synergism of interfacial coupling and hole-transfer, *Chem. Eng. J.* 382 (2020), 122840.
- [16] X. Wang, K. Maeda, A. Thomas, K. Takane, G. Xin, J.M. Carlsson, K. Domen, M. Antonietti, A metal-free polymeric photocatalyst for hydrogen production from water under visible light, *Nat. Mater.* 8 (2009) 76–80.
- [17] Z. Ouyang, Y. Yang, C. Zhang, S. Zhu, L. Qin, W. Wang, D. He, Y. Zhou, H. Luo, F. Qin, Recent advances in photocatalytic degradation of plastics and plastic-derived chemicals, *J. Mater. Chem. A* 9 (2021) 13402–13441.
- [18] D. Qin, Y. Zhou, W. Wang, C. Zhang, G. Zeng, D. Huang, L. Wang, H. Wang, Y. Yang, L. Lei, S. Chen, D. He, Recent advances in two-dimensional nanomaterials for photocatalytic reduction of CO<sub>2</sub>: insights into performance, theories and perspective, *J. Mater. Chem. A* 8 (2020) 19156–19195.
- [19] Y. Zhou, C. Zhang, D. Huang, W. Wang, Y. Zhai, Q. Liang, Y. Yang, S. Tian, H. Luo, D. Qin, Structure defined 2D Mo<sub>2</sub>C/2Dg-C<sub>3</sub>N<sub>4</sub> Van der Waals heterojunction: Oriented charge flow in-plane and separation within the interface to collectively promote photocatalytic degradation of pharmaceutical and personal care products, *Appl. Catal. B* 301 (2022), 120749.

- [20] D. He, C. Zhang, G. Zeng, Y. Yang, D. Huang, L. Wang, H. Wang, A multifunctional platform by controlling of carbon nitride in the core-shell structure: From design to construction, and catalysis applications, *Appl. Catal. B* 258 (2019), 117957.
- [21] B. Qiao, A. Wang, X. Yang, L.F. Allard, Z. Jiang, Y. Cui, J. Liu, J. Li, T. Zhang, Single-atom catalysis of CO oxidation using Pt1/FeOx, *Nat. Chem.* 3 (2011) 634–641.
- [22] Y. Wang, J. Mao, X. Meng, L. Yu, D. Deng, X. Bao, Catalysis with two-dimensional materials confining single atoms: concept, design, and applications, *Chem. Rev.* 119 (2019) 1806–1854.
- [23] X. Li, W. Bi, L. Zhang, S. Tao, W. Chu, Q. Zhang, Y. Luo, C. Wu, Y. Xie, Single-atom Pt as co-catalyst for enhanced photocatalytic H<sub>2</sub> evolution, *Adv. Mater.* 28 (2016) 2427–2431.
- [24] Y. Yang, G. Zeng, D. Huang, C. Zhang, D. He, C. Zhou, W. Wang, W. Xiong, B. Song, H. Yi, S. Ye, X. Ren, In situ grown single-atom cobalt on polymeric carbon nitride with bidentate ligand for efficient photocatalytic degradation of refractory antibiotics, *Small* 16 (2020), 2001634.
- [25] P. Sharma, S. Kumar, O. Tomanec, M. Petr, J. Zhu Chen, J.T. Miller, R.S. Varma, M. B. Gawande, R. Zbořil, Carbon nitride-based ruthenium single atom photocatalyst for CO<sub>2</sub> reduction to methanol, *Small* 17 (2021), 2006478.
- [26] B. Han, Y. Guo, Y. Huang, W. Xi, J. Xu, J. Luo, H. Qi, Y. Ren, X. Liu, B. Qiao, T. Zhang, Strong metal-support interactions between Pt single atoms and TiO<sub>2</sub>, *Angew. Chem. Int. Ed.* 59 (2020) 11824–11829.
- [27] H. Song, R. Du, Y. Wang, D. Zu, R. Zhou, Y. Cai, F. Wang, Z. Li, Y. Shen, C. Li, Anchoring single atom cobalt on two-dimensional MXene for activation of peroxymonosulfate, *Appl. Catal. B* 286 (2021), 119898.
- [28] S. Zhou, L. Shang, Y. Zhao, R. Shi, G.I.N. Waterhouse, Y.-C. Huang, L. Zheng, T. Zhang, Pd single-atom catalysts on nitrogen-doped graphene for the highly selective photothermal hydrogenation of acetylene to ethylene, *Adv. Mater.* 31 (2019), 1900509.
- [29] W. Xi, K. Wang, Y. Shen, M. Ge, Z. Deng, Y. Zhao, Q. Cao, Y. Ding, G. Hu, J. Luo, Dynamic co-catalysis of Au single atoms and nanoporous Au for methane pyrolysis, *Nat. Commun.* 11 (2020) 1919.
- [30] G. Wang, C.-T. He, R. Huang, J. Mao, D. Wang, Y. Li, Photoinduction of Cu single atoms decorated on UiO-66-NH<sub>2</sub> for enhanced photocatalytic reduction of CO<sub>2</sub> to liquid fuels, *J. Am. Chem. Soc.* 142 (2020) 19339–19345.
- [31] X. Hu, W. Zhang, X. Liu, Y. Mei, Y. Huang, Nanostructured Mo-based electrode materials for electrochemical energy storage, *Chem. Soc. Rev.* 44 (2015) 2376–2404.
- [32] M. Chen, Z. Wang, Y. Wang, Y. Li, Q. Chen, Sodium-ion storage mechanisms and design strategies of molybdenum-based materials: A review, *Appl. Mater. Today* 23 (2021), 100985.
- [33] D. Li, J. Shi, C. Li, Transition-Metal-Based Electrocatalysts as Cocatalysts for Photoelectrochemical Water Splitting: A Mini Review, *Small* 14 (2018), 1704179.
- [34] Y. Ma, T. Yang, H. Zou, W. Zang, Z. Kou, L. Mao, Y. Feng, L. Shen, S.J. Pennycook, L. Duan, X. Li, J. Wang, Synergizing Mo Single Atoms and Mo<sub>2</sub>C Nanoparticles on CNTs Synchronizes Selectivity and Activity of Electrocatalytic N<sub>2</sub> Reduction to Ammonia, *Adv. Mater.* 32 (2020), 2002177.
- [35] P. Du, K. Hu, J. Lyu, H. Li, X. Lin, G. Xie, X. Liu, Y. Ito, H.-J. Qiu, Anchoring Mo single atoms/clusters and N on edge-rich nanoporous holey graphene as bifunctional air electrode in Zn–air batteries, *Appl. Catal. B* 276 (2020), 119172.
- [36] L. Wang, X. Duan, X. Liu, J. Gu, R. Si, Y. Qiu, D. Shi, F. Chen, X. Sun, J. Lin, J. Sun, Atomically dispersed Mo supported on metallic Co<sub>9</sub>S<sub>8</sub> nanoflakes as an advanced noble-metal-free bifunctional water splitting catalyst working in universal pH conditions, *Adv. Energy Mater.* 10 (2020), 1903137.
- [37] R. Zhang, P. Li, F. Wang, L. Ye, A. Gaur, Z. Huang, Z. Zhao, Y. Bai, Y. Zhou, Atomically dispersed Mo atoms on amorphous g-C<sub>3</sub>N<sub>4</sub> promotes visible-light absorption and charge carriers transfer, *Appl. Catal. B* 250 (2019) 273–279.
- [38] X.-W. Guo, S.-M. Chen, H.-J. Wang, Z.-M. Zhang, H. Lin, L. Song, T.-B. Lu, Single-atom molybdenum immobilized on photoactive carbon nitride as efficient photocatalysts for ambient nitrogen fixation in pure water, *J. Mater. Chem. A* 7 (2019) 19831–19837.
- [39] Y. Cheng, S. Zhao, H. Li, S. He, J.-P. Veder, B. Johannessen, J. Xiao, S. Lu, J. Pan, M.F. Chisholm, S.-Z. Yang, C. Liu, J.G. Chen, S.P. Jiang, Unsaturated edge-anchored Ni single atoms on porous microwave exfoliated graphene oxide for electrochemical CO<sub>2</sub>, *Appl. Catal. B* 243 (2019) 294–303.
- [40] C. Zhang, D. He, S. Fu, G. Zeng, Q. Liang, Y. Yang, D. Huang, W. Wang, Y. Zhou, Silver iodide decorated ZnSn(OH)<sub>6</sub> hollow cube: Room-temperature preparation and application for highly efficient photocatalytic oxytetracycline degradation, *Chem. Eng. J.* 421 (2021), 129810.
- [41] Y. Wang, L. Li, Y. Wei, J. Xue, H. Chen, L. Ding, J. Caro, H. Wang, Water transport with ultralow friction through partially exfoliated g-C<sub>3</sub>N<sub>4</sub> nanosheet membranes with self-supporting spacers, *Angew. Chem. Int. Ed.* 56 (2017) 8974–8980.
- [42] G. Zhao, G. Liu, H. Pang, H. Liu, H. Zhang, K. Chang, X. Meng, X. Wang, J. Ye, Improved photocatalytic H<sub>2</sub> evolution over g-carbon nitride with enhanced in-plane ordering, *Small* 12 (2016) 6160–6166.
- [43] S. Guo, Z. Deng, M. Li, B. Jiang, C. Tian, Q. Pan, H. Fu, Phosphorus-doped carbon nitride tubes with a layered micro-nanostructure for enhanced visible-light photocatalytic hydrogen evolution, *Angew. Chem. Int. Ed.* 55 (2016) 1830–1834.
- [44] Y. Si, Z. Sun, L. Huang, M. Chen, L. Wu, A “ship-in-a-bottle” strategy to fabricate highly crystallized nanoporous graphitic C<sub>3</sub>N<sub>4</sub> microspheres under pressurized conditions, *J. Mater. Chem. A* 7 (2019) 8952–8959.
- [45] H. Wang, Q. Lin, L. Yin, Y. Yang, Y. Qiu, C. Lu, H. Yang, Biomimetic design of hollow flower-like g-C<sub>3</sub>N<sub>4</sub>@PDA organic framework nanospheres for realizing an efficient photoreactivity, *Small* 15 (2019), 1900011.
- [46] X. Liang, G. Wang, X. Dong, G. Wang, H. Ma, X. Zhang, Graphitic carbon nitride with carbon vacancies for photocatalytic degradation of bisphenol A, *ACS Appl. Nano Mater.* 2 (2019) 517–524.
- [47] W. Tu, Y. Xu, J. Wang, B. Zhang, T. Zhou, S. Yin, S. Wu, C. Li, Y. Huang, Y. Zhou, Z. Zou, J. Robertson, M. Kraft, R. Xu, Investigating the role of tunable nitrogen vacancies in graphitic carbon nitride nanosheets for efficient visible-light-driven H<sub>2</sub> evolution and CO<sub>2</sub> reduction, *ACS Sustain. Chem. Eng.* 5 (2017) 7260–7268.
- [48] W. Wang, Z. Zeng, G. Zeng, C. Zhang, R. Xiao, C. Zhou, W. Xiong, Y. Yang, L. Lei, Y. Liu, D. Huang, M. Cheng, Y. Yang, Y. Fu, H. Luo, Y. Zhou, Sulfur doped carbon quantum dots loaded hollow tubular g-C<sub>3</sub>N<sub>4</sub> as novel photocatalyst for destruction of *Escherichia coli* and tetracycline degradation under visible light, *Chem. Eng. J.* 378 (2019), 122132.
- [49] P. Zhou, F. Lv, N. Li, Y. Zhang, Z. Mu, Y. Tang, J. Lai, Y. Chao, M. Luo, F. Lin, J. Zhou, D. Su, S. Guo, Strengthening reactive metal-support interaction to stabilize high-density Pt single atoms on electron-deficient g-C<sub>3</sub>N<sub>4</sub> for boosting photocatalytic H<sub>2</sub> production, *Nano Energy* 56 (2019) 127–137.
- [50] G. Kresse, J. Hafner, Ab initio molecular-dynamics simulation of the liquid-metal–amorphous-semiconductor transition in germanium, *Phys. Rev. B* 49 (1994) 14251–14269.
- [51] G. Kresse, J. Furthmüller, Efficient iterative schemes for ab initio total-energy calculations using a plane-wave basis set, *Phys. Rev. B* 54 (1996) 11169–11186.
- [52] P.E. Blöchl, Projector augmented-wave method, *Phys. Rev. B* 50 (1994) 17953–17979.
- [53] G. Kresse, D. Joubert, From ultrasoft pseudopotentials to the projector augmented-wave method, *Phys. Rev. B* 59 (1999) 1758–1775.
- [54] B. Hammer, L.B. Hansen, J.K. Nørskov, Improved adsorption energetics within density-functional theory using revised Perdew–Burke–Ernzerhof functionals, *Phys. Rev. B* 59 (1999) 7413–7421.
- [55] H.J. Monkhorst, J.D. Pack, Special points for Brillouin-zone integrations, *Phys. Rev. B* 13 (1976) 5188–5192.
- [56] G.W.T.M.J. Frisch, H.B. Schlegel, G.E. Scuseria, M.A. Robb, J.R. Cheeseman, G. Scalmani, V. Barone, G.A. Petersson, H. Nakatsuji, X. Li, M. Caricato, A. V. Marenich, J. Bloino, B.G. Janesko, R. Gomperts, B. Mennucci, H.P. Hratchian, J. V. Ortiz, A.F. Izmaylov, J.L. Sonnenberg, D. Williams-Young, F. Ding, F. Lipparini, F. Egidi, J. Goings, B. Peng, A. Petrone, T. Henderson, D. Ranasinghe, V. G. Zakrzewski, J. Gao, N. Rega, G. Zheng, W. Liang, M. Hada, M. Ehara, K. Toyota, R. Fukuda, J. Hasegawa, M. Ishida, T. Nakajima, Y. Honda, O. Kitao, H. Nakai, T. Vreven, K. Throssell, J.A. Montgomery Jr., J.E. Peralta, F. Ogliaro, M. J. Bearpark, J.J. Heyd, E.N. Brothers, K.N. Kudin, V.N. Staroverov, T.A. Keith, R. Kobayashi, J. Normand, K. Raghavachari, A.P. Rendell, J.C. Burant, S.S. Iyengar, J. Tomasi, M. Cossi, J.M. Millam, M. Klene, C. Adamo, R. Cammi, J.W. Ochterski, R.L. Martin, K. Morokuma, O. Farkas, J.B. Foresman, D.J. Fox, *Gaussian 16 Rev. C.01*, Gaussian Inc., Wallingford CT, 2016.
- [57] T. Lu, F. Chen, Multiwfn: A multifunctional wavefunction analyzer, *J. Comput. Chem.* 33 (2012) 580–592.
- [58] A.D. Becke, Density-functional thermochemistry. III, role Exact. Exch., *J. Chem. Phys.* 98 (1993) 5648–5652.
- [59] C. Lee, W. Yang, R.G. Parr, Development of the Colle–Salvetti correlation-energy formula into a functional of the electron density, *Phys. Rev. B* 37 (1988) 785–789.
- [60] W.R. Wadt, P.J. Hay, Ab initio effective core potentials for molecular calculations. Potentials for main group elements Na to Bi, *J. Chem. Phys.* 82 (1985) 284–298.
- [61] P.J. Hay, W.R. Wadt, Ab initio effective core potentials for molecular calculations. Potentials for the transition metal atoms Sc to Hg, *J. Chem. Phys.* 82 (1985) 270–283.
- [62] J. Fu, J. Yu, C. Jiang, B. Cheng, g-C<sub>3</sub>N<sub>4</sub>-based heterostructured photocatalysts, *Adv. Energy Mater.* 8 (2018), 1701503.
- [63] Y. Zhou, W. Wang, C. Zhang, D. Huang, C. Lai, M. Cheng, L. Qin, Y. Yang, C. Zhou, B. Li, H. Luo, D. He, Sustainable hydrogen production by molybdenum carbide-based efficient photocatalysts: From properties to mechanism, *Adv. Colloid Interface Sci.* 279 (2020), 102144.
- [64] Z. Mo, X. Zhu, Z. Jiang, Y. Song, D. Liu, H. Li, X. Yang, Y. She, Y. Lei, S. Yuan, H. Li, L. Song, Q. Yan, H. Xu, Porous nitrogen-rich g-C<sub>3</sub>N<sub>4</sub> nanotubes for efficient photocatalytic CO<sub>2</sub> reduction, *Appl. Catal. B* 256 (2019), 117854.
- [65] C. Zhou, P. Xu, C. Lai, C. Zhang, G. Zeng, D. Huang, M. Cheng, L. Hu, W. Xiong, X. Wen, L. Qin, J. Yuan, W. Wang, Rational design of graphitic carbon nitride copolymers by molecular doping for visible-light-driven degradation of aqueous sulfamethazine and hydrogen evolution, *Chem. Eng. J.* 359 (2019) 186–196.
- [66] Z. Chen, T.-T. Fan, X. Yu, Q.-L. Wu, Q.-H. Zhu, L.-Z. Zhang, J.-H. Li, W.-P. Fang, X.-D. Yi, Gradual carbon doping of graphitic carbon nitride towards metal-free visible light photocatalytic hydrogen evolution, *J. Mater. Chem. A* 6 (2018) 15310–15319.
- [67] Z. Wang, Y. Huang, M. Chen, X. Shi, Y. Zhang, J. Cao, W. Ho, S.C. Lee, Roles of N-vacancies over porous g-C<sub>3</sub>N<sub>4</sub> microtubes during photocatalytic NO<sub>x</sub> removal, *ACS Appl. Mater. Interfaces* 11 (2019) 10651–10662.
- [68] Y. Yang, G. Zeng, D. Huang, C. Zhang, D. He, C. Zhou, W. Wang, W. Xiong, X. Li, B. Li, W. Dong, Y. Zhou, Molecular engineering of polymeric carbon nitride for highly efficient photocatalytic oxytetracycline degradation and H<sub>2</sub>O<sub>2</sub> production, *Appl. Catal. B* 272 (2020), 118970.
- [69] C. Zhang, W. Wang, A. Duan, G. Zeng, D. Huang, C. Lai, X. Tan, M. Cheng, R. Wang, C. Zhou, W. Xiong, Y. Yang, Adsorption behavior of engineered carbons and carbon nanomaterials for metal endocrine disruptors: Experiments and theoretical calculation, *Chemosphere* 222 (2019) 184–194.
- [70] L. Han, X. Liu, J. Chen, R. Lin, H. Liu, F. Lü, S. Bak, Z. Liang, S. Zhao, E. Stavitski, J. Luo, R.R. Adzic, H.L. Xin, Atomically dispersed molybdenum catalysts for efficient ambient nitrogen fixation, *Angew. Chem. Int. Ed.* 58 (2019) 2321–2325.
- [71] W. Wang, Q. Niu, G. Zeng, C. Zhang, D. Huang, B. Shao, C. Zhou, Y. Yang, Y. Liu, H. Guo, W. Xiong, L. Lei, S. Liu, H. Yi, S. Chen, X. Tang, 1D porous tubular g-C<sub>3</sub>N<sub>4</sub>

- capture black phosphorus quantum dots as 1D/0D metal-free photocatalysts for oxytetracycline hydrochloride degradation and hexavalent chromium reduction, *Appl. Catal. B* 273 (2020), 119051.
- [72] H. Funke, A.C. Scheinost, M. Chukalina, Wavelet analysis of extended x-ray absorption fine structure data, *Phys. Rev. B* 71 (2005), 094110.
- [73] W. Chen, J. Pei, C.-T. He, J. Wan, H. Ren, Y. Zhu, Y. Wang, J. Dong, S. Tian, W.-C. Cheong, S. Lu, L. Zheng, X. Zheng, W. Yan, Z. Zhuang, C. Chen, Q. Peng, D. Wang, Y. Li, Rational Design of Single Molybdenum Atoms Anchored on N-Doped Carbon for Effective Hydrogen Evolution Reaction, *Angew. Chem. Int. Ed.* 56 (2017) 16086–16090.
- [74] W. Yang, R.G. Parr, Hardness, softness, and the Fukui function in the electronic theory of metals and catalysis, *Proc. Natl. Acad. Sci. U. S. A.* 82 (1985) 6723–6726.
- [75] H. Chauhan, Y. Kumar, J. Dana, B. Satpati, H.N. Ghosh, S. Deka, Photoinduced ultrafast charge separation in colloidal 2-dimensional CdSe/CdS-Au hybrid nanoplatelets and corresponding application in photocatalysis, *Nanoscale* 8 (2016) 15802–15812.
- [76] J. Di, X. Zhao, C. Lian, M. Ji, J. Xia, J. Xiong, W. Zhou, X. Cao, Y. She, H. Liu, K. P. Loh, S.J. Pennycook, H. Li, Z. Liu, Atomically-thin Bi<sub>2</sub>MoO<sub>6</sub> nanosheets with vacancy pairs for improved photocatalytic CO<sub>2</sub> reduction, *Nano Energy* 61 (2019) 54–59.
- [77] L.K. Putri, B.-J. Ng, W.-J. Ong, H.W. Lee, W.S. Chang, S.-P. Chai, Engineering nanoscale p-n junction via the synergetic dual-doping of p-type boron-doped graphene hybridized with n-type oxygen-doped carbon nitride for enhanced photocatalytic hydrogen evolution, *J. Mater. Chem. A* 6 (2018) 3181–3194.
- [78] W.-T. Tsai, C.-W. Lai, T.-Y. Su, Adsorption of bisphenol-A from aqueous solution onto minerals and carbon adsorbents, *J. Hazard. Mater.* 134 (2006) 169–175.
- [79] D. Qiao, Z. Li, J. Duan, X. He, Adsorption and photocatalytic degradation mechanism of magnetic graphene oxide/ZnO nanocomposites for tetracycline contaminants, *Chem. Eng. J.* 400 (2020), 125952.
- [80] L. Duan, L. Li, Z. Xu, W. Chen, Adsorption of tetracycline to nano-NiO: the effect of co-existing Cu(II) ions and environmental implications, *Environ. Sci. -Process Impacts* 16 (2014) 1462–1468.
- [81] X. Liu, W. Zhang, M. Peng, G. Zhai, L. Hu, L. Mao, The role of S and Mo doping on the dissociation of water molecule on FeOCl surface: Experimental and theoretical analysis, *Chem. Eng. J.* 426 (2021), 131353.
- [82] Z. Zeng, Y. Su, X. Quan, W. Choi, G. Zhang, N. Liu, B. Kim, S. Chen, H. Yu, S. Zhang, Single-atom platinum confined by the interlayer nanospace of carbon nitride for efficient photocatalytic hydrogen evolution, *Nano Energy* 69 (2020), 104409.
- [83] C. Zhang, S. Tian, F. Qin, Y. Yu, D. Huang, A. Duan, C. Zhou, Y. Yang, W. Wang, Y. Zhou, H. Luo, Catalyst-free activation of permanganate under visible light irradiation for sulfamethazine degradation: Experiments and theoretical calculation, *Water Res.* 194 (2021), 116915.
- [84] P. Chen, L. Blaney, G. Cagnetta, J. Huang, B. Wang, Y. Wang, S. Deng, G. Yu, Degradation of Ofloxacin by Perylene Diimide Supramolecular Nanofiber Sunlight-Driven Photocatalysis, *Environ. Sci. Technol.* 53 (2019) 1564–1575.
- [85] F. Wang, Y. Feng, P. Chen, Y. Wang, Y. Su, Q. Zhang, Y. Zeng, Z. Xie, H. Liu, Y. Liu, W. Lv, G. Liu, Photocatalytic degradation of fluoroquinolone antibiotics using ordered mesoporous g-C<sub>3</sub>N<sub>4</sub> under simulated sunlight irradiation: Kinetics, mechanism, and antibacterial activity elimination, *Appl. Catal. B* 227 (2018) 114–122.
- [86] F. Qin, Y. Peng, G. Song, Q. Fang, R. Wang, C. Zhang, G. Zeng, D. Huang, C. Lai, Y. Zhou, X. Tan, M. Cheng, S. Liu, Degradation of sulfamethazine by biochar-supported bimetallic oxide/persulfate system in natural water: Performance and reaction mechanism, *J. Hazard. Mater.* 398 (2020), 122816.